SLAC-PUB-3222
CALT-68-1076
December, 1983
(I)

THE MARK III SPECTROMETER*

D. Bernstein, J. Bernstein, K. Bunnell, G. Burgueno, R. Cassell
B. Collins, D. Coward, K. Einsweiler, R. Eisele, B. Haber [1] ,
D. Hutchinson, G. Mazaheri, E. McNerney, L. Moss, R. Mozley,
A. Odian, J. Roehrig [2] , K. Skarpaas, B. Sukiennicki, W. Toki,
Y. Unno [3] , F. Villa, W. Wadley, N. Wermes, D. Wisinski.
Stanford Linear Accelerator Center
Stanford University, Stanford , California 94305

R. Baltrusaitis [4] , G. Belyansky, D. Coffman, R. Cooper,
W. Freidler, H. Grau, J. Hauser, D. Hitlin,
J. Richman, J. Russell, R. Schindler.
California Institute of Technology
Pasadena, California 91125

J. Becker, G. Blaylock, H. Cui [5] , B. Eisenstein, G. Gladding,
J. Kohlmeier, S. Plaetzer, V. Simaitis, A. Spadafora, J. Thaler,
A. Wattenberg, W. Wisniewski.
University of Illinois
Urbana, Illinois 61801

H. Bledsoe, D. Dorfan, R. Fabrizio [6] , F. Grancagnolo [7] , R. Hamilton,
C. Heusch, W. Nilsson, J. Perrier, W. Rowe, H. Sadrozinski,
M. Scarlatella, T. Schalk, A. Seiden, D. B. Smith [8] .
University of California at Santa Cruz
Santa Cruz, California 95064

J. Brown, T. Burnett, V. Cook, C. Del Papa [9] , A. Duncan,
D. Forbush, H. Guldenmann, P. Mockett, A. Nappi [10] ,
J. Sleeman, F. Toeus, H. Willutzki.
University of Washington
Seattle, Washington 98195

Submitted to Nuclear Instruments and Methods

---

* Work supported in part by the Department of Energy, contract DE-AC03-76SF00515 DE-AC03-76-ER01195, DE-AC03-81-ER40050 and DE-AM03-76SF00034

ABSTRACT

This paper describes the design, construction and performance of the Mark III, a new general purpose large solid angle spectrometer at SPEAR, the SLAC 2 - 8 GeV e^+e^- storage ring. The detector has been designed for the study of exclusive final states in e^+e^- annihilation, which requires large solid angle coverage combined with charged particle momentum resolution, particle identification, and photon detection efficiency at low energies.

Present address:

1. Physics Dept. Bar-Ilan Univ., Ramat-Gan, Israel
2. Xonics Imaging, 274 El Sobrante Way, Sunnyvale, Calif.
3. Natl. Lab. for High Energy Physics, Ibaraki-Sen, 305 Japan
4. Physics Dept. Univ. of Utah, Salt Lake City, Utah
5. Institute of High Energy Physics, Beijing, China
6. Applied Technology, P.O. Box 478, Sunnyvale, Calif.
7. CERN, EP, 1211 Geneve 23, Switzerland
8. Atari Inc., 30 East Plumeria Drive, San Jose, Calif.
9. INFN, Sezione di Bologna, Bologna, Italy
10. Visiting from the University of Pisa, Pisa, Italy

1. Introduction

The Mark III spectrometer is a new general purpose detector at SPEAR designed for the low energy region of charmed particle physics. Design emphasis was placed on the complete reconstruction of exclusive hadronic states, which requires large solid angle systems to identify leptons and hadrons, and low energy photon detection efficiency to allow the efficient reconstruction of π^0 and η mesons.

Design of the detector started in 1978 using as a base the flux return steel of the original SPEAR magnetic detector, Mark I. It was decided to build a new coil of greater thickness and larger inner diameter than the previous one, allowing the shower counter for photon detection to be inside the coil and reducing power consumption. The shower counters for both of the earlier SPEAR magnetic spectrometers (Mark I and Mark II) had been outside their coils, reducing their low energy photon sensitivity.

Construction was completed in the spring of 1981 and Mark III was installed at SPEAR that summer. Check out started during the fall and the first data was taken in the spring of 1982. The following is a report on the design, the construction techniques and the performance obtained during the first data taking runs. End and side views of the spectrometer are shown in Figs. 1 and 2.

2. Magnet

The use of the flux return steel of the original SPEAR magnetic detector set the scale for the entire project. The new coil was designed to produce a field of 0.4 Tesla at the center of the spectrometer. In order to make possible the detection of low energy photons, the electromagnetic shower counters were placed in front of the coil, rather than behind as in most previous designs. This allowed the use of a thick coil with 1 MW of power consumption rather than the 2 MW of the previous SPEAR detectors. The coil was designed with four layers of 5 cm by 5 cm aluminum conductor with a 2.5 cm diameter water passage. All power and water connections were made at the ends of the coil, with the layers

connected in series electrically and in parallel for water flow.

The coil was wound on a 2.24 cm thick aluminum spool of 1.715 meter inner radius which acts as a shorted secondary turn helping slow down the rate of change of magnetic field in case of an unexpected crash of the power supply.

For winding, the spool was mounted on a multiarm mandrel which rotated about its longitudinal axis. The dead soft conductor was wrapped with tape and coated with thermo-setting epoxy and then wound two turns at a time onto the spool. Additional insulation (Dacron-Mylar-Dacron) was placed between layers. After completion of the fourth layer, the coil was covered with a layer of epoxied fiberglass and then cured by covering with thermal insulation and heating with a small electrical current without water cooling.

The coil was mounted inside the flux return on four coplanar supports designed to allow expansion of the coil due to temperature changes.

In operating a solenoid such as this on a storage ring it is necessary to compensate for the effect of the axial magnetic field on the beam. This was done by installing small diameter solenoids at each end of the main solenoid and powering them to give a line integral of field opposite that of the main solenoid. The compensators are built into the end cap flux return iron and, having the same number of turns as the main solenoid, they can be powered in series with the main coil.

After mounting the end steel and compensators, the magnetic field was measured using three Hall probes mounted on an arm which could be rotated about the magnetic axis. The probes were aligned to measure the radial and longitudinal (Z) field components and could be moved radially, azimuthally, and longitudinally. The measured fields were fitted with polynomials making use of the reflection and rotational symmetry of the magnetic field. 17 parameters were required to describe the field to an accuracy of about 0.2% over the volume of the tracking chamber.

3. Beam Pipe and Multiple Scattering

At SPEAR energies average particle momenta are below 500 MeV/c. Multiple coulomb scattering is therefore a major source of measurement error. In order to reduce the multiple scattering, a thin walled 1.5 mm beryllium pipe was used. The amount of radiation lengths of material traversed by particles is given in Table 1. The total, 0.0214 r.l., contributes 1.5% to the momentum measurement error, $\Delta p/p$, of the drift chamber.

4. Inner Trigger Chamber (Layer 1)

Previous large magnetic detectors at SPEAR had used thin scintillation counters mounted around the beam pipe at the interaction region to define the location and time of the interaction and thus reduce triggers from cosmic rays. Not only do such scintillation counters cause appreciable multiple scattering but it is difficult to find a path for light guides to the exterior of the magnet. As a result it was decided to use a thin walled drift chamber for this purpose.

The chamber consists of 4 layers, each of 32 drift cells, forming concentric cylinders about 20 cm in diameter and 110 cm long. Field wires of 178 μm BeCu separate the cells. The sense wires, of 38 μm stainless steel to allow Z position determination by charge division, are offset by half a cell in alternate layers Fig. 3(a). Two of the four layers are incorporated in the trigger; the other two are used only for tracking.

The gas used in the chamber is a 70% argon, 30% ethane mixture which flows through without recirculation at a rate of about 5 volume changes per day.

Because of the half cell offset, the sum of drift distances of a radial track in two radially adjacent cells is approximately constant Fig. 3(b). By feeding the output signals from these wires into opposite ends of a tapped delay line chronotron circuit [1], coincidences can be obtained during a time much shorter than the maximum drift time. The chronotron is a series of coincidence circuits connected by delay lines to give a total delay time equal to the maximum drift time. The signals travelling in opposite directions through the delay lines must

meet in one of the coincidence circuits. The coincidence gate width is determined by the tap interval, by the inequality of cell size, and by drift velocity variations.

For use in the chronotron, signals from both ends of each wire are discriminated and "Or'd" to remove the effects of the large pulse height variations which occur as a function of position along the resistive wire. The shaped output pulse is then introduced at one end of the tapped chronotron delay line.

While the total drift time in the cell is 250 nsec, the gate for the output of the chronotron circuit can be $\approx$100 nsec long. Thus the cosmic ray triggers are reduced by a factor of 2.5 compared to operation without the chronotron. Since beam crossings at SPEAR occur every 780 nsec, the total reduction is $\approx$8. The total area subtended by the chamber is made as small as possible so as to reduce the cosmic ray rate. The Z information can be used both on-line and off-line further to select particles coming from the interaction region. Figure 4 shows the chronotron resolution for reconstructed hadrons which are accepted by a 100 nsec gate.

5. Main Drift Chamber [2]

The main drift chamber, 2.29 meters in diameter and 3.34 meters long, directly surrounds the trigger chamber. The chamber consists of two sections, an inner region, Layer 2, with a high density of signal wires and a larger outer portion, Layers 3 - 8. General physical characteristics are listed in Table 2.

a. Layer 2

This region consists of 32 cells in azimuth, each containing 13 sense wires of 20 μm diameter tungsten and two 57 μm diameter stainless steel guard wires. The radial spacing for these fifteen wires is 1 cm. The stainless steel wires are used to determine the longitudinal position by means of the induced current from the neighboring sense wires. Separating the cells are an equal number of BeCu field wires of 175 μm diameter (Figs. 5 and 6).

This part of the chamber is operated at low gas gain ($\approx 2 \times 10^4$) to avoid saturation and thus make dE/dx measurement possible. The high density of wires

in this region also aids in the detection and reconstruction of charged and neutral decays. The layer covers a larger solid angle than the time of flight counters, 93% rather than 80% of 4π and hence is particularly useful for particle identification at small angles. Alternate sense wires are staggered in ϕ by ± 150 μm to aid in resolving the left-right ambiguity.

A problem caused by the high density of sense wires is the presence of pulses of opposite polarity induced by signals on neighboring sense wires. These signals are compensated by the use of coupling resistors between neighboring wires to feed negative polarity signals of the proper size to remove the positive induced signal.

b. Layers $3-8$

The 6 outer layers of the chamber, 3 through 8, are made up of $16 \times$ N cells (where N is the layer number) with each cell containing three tungsten sense wires of 20 μm diameter. The spacing is chosen to allow all cells regardless of layer to be the same size. In these layers the central of the three sense wires is offset relative to the other two by $\pm 400\mu$m, again to allow resolution of the ambiguity. Radially on either side of the sense wires are stainless steel guard wires used in charge division to determine Z position in layers 3, 5, and 7. The 5 field wires separating the cells are 175 μm BeCu. Layers 4 and 6 are in 7.7 and -9.0 degree stereo respectively.

c. Chamber Gas

The chamber uses an 89% argon, 10% CO_2, 1% methane gas mixture. The choice of mixture is critical since the high electric field on the field wires makes possible the growth of carbon "whiskers" if certain organic compounds are present in large quantity. A flow-through system is used at a rate of about one volume change per day.

d. Electronics

The discriminators and amplifiers for all of the drift chambers are located in a concrete walled radiation shielded alcove close to the spectrometer. They are coupled to the drift chamber wires via 13.5 m long coaxial cables that are

additionally shielded against electrical pickup from magnet power supply noise and beam induced radio frequency noise. Although the beam pipe is thick in skin depth and continuous near the interaction region, there are many locations in the SPEAR ring where ceramic insulators allow beam induced signals to leave the interior and run on the exterior of the beam pipe. Pickup of this signal was strong on the leads of the inner layers. For layer 2 it was necessary to add preamplifier circuits on the face of the chamber since it had a gas gain 1/10 that of the outer layers and a signal of only 200 μV. Electronics schematics for layer 2 and layers 3 - 8 are shown in Figs. 7 and 8.

e. Chamber Operation

A method of illustrating the intrinsic accuracy of the chamber is to examine drift times from a single 3 wire layer. The plot of (T1+T3)/2-T2 is shown in Fig. 9 where the T's represent the arrival time of signals at the respective wires. The two groups of hits result from the offset of the central wire, with the sign giving the side of the cell on which the track passed. The region between the peaks comes from tracks which cross the center line of a cell. The separation of the two peaks corresponds to twice the offset of the central wire. The 2 mm separation of the two peaks as shown in Fig. 9 is somewhat more than the nominal value, due to the electrostatic forces separating the wires. The width of the peaks corresponds to a resolution of 220 μm per wire. This resolution (for layer 5) includes the effects of the longitudinal (Z) position and is averaged over all cells in the layer. It is the best obtained without correction for Z position and individual cell variation. Corrections are made for the non-linear drift velocity as a function of position and for the Lorentz angle of electron drift in the magnetic field.

In track fitting, the 3 wire cell configuration allows the construction, with a precision of $\approx$ 10 mrad, of track vectors in each cell which is hit. The vector from a single cell can determine whether the particle in question could have come from the interaction region and whether it can be joined as a track to other vectors. Initial fitting is done in the axial projection using the non-stereo layers. Then the stereo layers are examined to find which cells fit the candidate tracks. In this

selection the positions along the wires found by charge division are useful, since the Z accuracy of the charge division is sufficient to determine which stereo cell is a reasonable candidate.

Individual cell efficiencies were determined by leaving cells out of the trigger and fitting procedures and then checking to see if a hit occurred. By doing this at different voltages the best operating point could be determined. Figure 10 shows a plot of efficiency per cell indicating that individual cells have an efficiency of about 97% for having at least 2 wires hit.

Tracks were fitted to a helix in the magnetic field and residuals for individual cells obtained by leaving them out of the fit. Figure 11 shows these residuals. The momentum resolution without using a vertex constraint can be expressed as:

$$\left(\frac{\Delta p}{p}\right)^2 = 0.015^2 + (0.015p)^2.$$

The first term is due to multiple scattering in the chamber gas and wires. The difference between the measured and calculated momentum of muon pair members is shown in Fig. 12, while Figs. 13 and 14 show the ϕ and λ accuracy for these tracks, where ϕ is the azimuth and λ the dip angle.

Charge division gives the position of the hit to better than 1% (σ) of the wire length on the outer layers 5 and 7 but only to 3% on layer 3 where electromagnetic pickup is strong. This Z position information is used primarily in pattern recognition but is also used to give a dip angle of limited precision for those tracks at too small an angle with respect to the beams to intercept the inner stereo layer (layer 4). The accuracy of the charge division measurement is also reduced by thermal noise due to cable capacitance and by signals induced by tracks in neighboring cells.

The twelve dE/dx measurements in layer 2 provide useful separation of low energy kaons and pions as shown in Fig. 15. Twelve measurements of ionization are made in layer 2 and the larger third are removed to reduce the Landau fluctuations.

6. Time of Flight Counters [3]

The time of flight counters consist of 48 scintillation counters 15.6 cm wide and 3.2 m long made of Nuclear Enterprises Pilot F. They are mounted on the outer cylindrical surface of the drift chamber at a radius of 1.2 m from the interaction region, allowing an 80% coverage of the total solid angle.

a. Counters

The counters were made as thick as possible (5 cm) given the available space and the desirablity of matching the cross sectional area of the scintillator to the 16 square centimeter area of the photomultiplier photocathodes. The light pipes are tapered to a width of 7.5 cm as they pass through the iron end plates.

Tapering reduces the area for transmitting light and correspondingly increases the average angle of light. If the tapering were done a long distance before the light reaches the photomultiplier the spread in time of the light arrival would be increased. Therefore a minimum taper was used to pass through the iron and the light pipes then continued at the 7.5 cm width until a fast taper in the form of a cone was made at the photomultiplier. See Fig. 16.

A monte-carlo simulation of a counter showed that the mean number of reflections for light reaching the photo-cathode is 20 while the mean number of reflections for the first photon is 6.

The photomultipliers are joined to the light guides by a transparent "cookie", a slightly flexible disk 4 cm in diameter and 3 mm thick, made of 40 parts of Dow Corning Sylguard 184, 1 part 184 hardener, and 3 parts of Dow Corning 200. The photomultiplier used is the Amperex XP2020, chosen because of the small transit time variations across the face of its photocathode. The photomultipliers are mounted just outside the steel end plates in a region of low magnetic field ($\approx$ 1 gauss). They are shielded by concentric cylinders of mu-metal and soft iron, which reduce the field at the photocathode to about 0.1 gauss. The anode signal cables used for time of flight measurement are 75 m long and are mounted in temperature controlled ducts to reduce transit time variations.

b. Electronics

The discriminators are identical to those developed for the Mark II [4]. They measure the time at two thresholds as well as the total pulse height. Signals from the photomultiplier anodes are used for time measurement while the outputs of the dynodes are used in the trigger. Time measurements are made relative to a beam pick up signal from the storage ring.

The electronics is calibrated using signals from a mercury switch pulser, a series of remotely switched precise delays, and a variable high voltage. The entire system is checked periodically with a free running N_2 laser light pulser driving quartz fiber light guides to deposit light pulses in the center of each scintillator. Calibration timing is done with respect to the output of a vacuum photodiode which is exposed to the same laser.

Final calibration is done by means of Bhabha scattered e^+e^- pairs. Corrections are made for the time of light passage in the scintillator, the gain and transit time of the photomultiplier, the variation in pulse height, and the different cable lengths. The longitudinal position of the particles traversing the counters can be obtained from relative times at either end of the scintillator and from drift chamber track information.

c. Performance

Figure 17 shows a plot of the difference of Bhabha times corrected for position and pulse height and the predicted value from path lengths alone. This plot, summed over the 48 counters, shows a σ of 171 picoseconds. The resolution obtained for hadronic events is 189 picoseconds.

Figure 18 is a scatter plot of β vs momentum for tracks from hadronic ψ decays, showing a clear separation of e, π, K, and p components.

7. Shower Counters

Two configurations of shower counters are used, a cylindrical ("barrel") counter surrounding the drift chamber, inside the coil to allow good low energy gamma ray detection efficiency, and two end cap shower counters mounted on removable steel doors. Both types consist of 24 layers of proportional cells separated by 0.5 radiation length aluminum clad lead sheets.

a. Barrel Shower Counter [5]

In order not to waste radial space between the drift chamber and the coil, and to avoid inevitable dead regions between separate modules, the barrel shower counter is constructed as a uniform cylindrical annulus. It consists of a 3.85 m long, 2.52 m diameter, 2.3 cm thick aluminum spool on which are mounted 23 layers of 0.28 cm (1/2 radiation length) lead spaced 1.27 cm apart radially as shown in Fig. 19.

To give strength for the support of sheets of this thickness, an alloy of 6% antimony, 94% lead was used, reinforced by epoxying 0.064 cm aluminum sheets on each side. These were fabricated in ten 36 degree sectors.

The layers are supported radially by 5 longitudinally spaced circular aluminum ribs which are grooved to allow placement of stainless steel bands. In constructing a layer, the ten sectors are put in place with the ribs attached to the exterior of the lead sheets. The sheets are given a weak attachment to the ribs of the previous layer until the new layer is complete. Stainless steel bands are then tightened around the five ribs to support the load of the new lead layer.

The gas region is divided into 320 cells circumferentially by thin aluminum I shaped barriers. In the center of each cell a stainless steel wire is strung axially, passing through insulated holes in the ribs, which also provide for the gas circulation. This assembly is mounted inside the coil suspended radially by 24 stainless steel bolts attached to the magnet steel. Specifications for the counter are given in Table 3.

b. End Cap Shower Counters [6]

The functional design of the end cap shower counter is the same as that of the barrel counter: 24 layers of 0.5 radiation length lead with 1.17 cm gaps. Extruded rectangular aluminum tubes 2.71 cm wide by 1.17 cm thick support the lead sheets in a 24 layer sandwich held together by epoxy. Stainless steel sense wires are supported at the ends of each tube by rectangular inserts which also provide a gas seal. Gas is introduced through holes in the tubes and the intervening lead which direct the gas through alternate ends of the tubes inward and then out again through similar openings. Specifications are given in Table 4.

The steel doors are circular, with a large central slot to clear the compensator magnet and its support stand. To fit this shape, each end cap shower counter is made in 5 parts. Three of these are fitted on the door and two smaller units are mounted behind the compensator support as shown in Fig. 20.

The gas mixture used for both barrel and end cap counters is 20% methane 80% argon, flowed through at a rate of one volume change per day.

Specifications for the end cap counters are given in Table 4.

c. Electronics

Signals from both ends of every wire in the first 6 layers of the shower counter are read out individually, while the next 18 layers are read in groups of 3 radially. The sense wires are isolated from the electronics by 25 nf capacitors, and are operated at about 2100 volts. The signals are read onto combined amplifier and sample and hold circuits (ISHAMs) mounted 24 to a card in crates supported on the exterior of the spectrometer. The close location saved cable costs and also reduces the capacitive noise by making the input cables as short as possible. Figure 21. is a schematic of the electronics.

The charge division measurement of Z position is accurate to 0.8% of the wire length. The stored information is strobed by the trigger signal to a Brilliant ADC (BADC [7]) for pedestal subtraction and gain correction.

d. Performance

A plot of shower energy as a function of Z in Fig. 22 clearly shows the effect of the ribs. Using muon pairs and Bhabha electrons, position resolutions of 7 mr in ϕ and 2.7 cm in Z ($\approx$20 mr in θ) have been obtained as shown in Figs. 23 and 24.

Energy resolution and linearity can be studied using Bhabha scattered electrons in the higher energy region and kinematically constrained π^os produced in $\psi \rightarrow \pi^+\pi^-\pi^0$ decay in the lower energy region. Figures 25 (a) and (b) show the energy linearity and Fig. 26 the energy resolution for Bhabha scattered electrons at the ψ. A value of ΔE / E of $17\%/\sqrt{E}$ (E in GeV) has been obtained.

Detection efficiency for low energy photons is explored by again using constrained π^o photons from $\psi \rightarrow \pi^+\pi^-\pi^0$. Figure 27 shows a plot of efficiency vs energy obtained by this method with a 70% efficiency for 50 MeV photons.

Figure 28 shows a $\gamma\gamma$ mass plot for neutrals from events satisfying a constrained fit to the reaction $\psi \rightarrow \gamma\gamma\gamma\pi^+\pi^-$. The π^o and η are easily seen. It has proven possible to reconstruct events with up to 5 photons.

8. The Muon Detection System

The muon detection system is placed outside the octagonal steel flux return. Each of its eight sides consists of two layers separated by steel plates about 13 cm thick. The layers consist of proportional counter tubes 2.5 cm in radius in an overlapping arrangement (Fig. 29) allowing hits to be located to $\pm$9 mm in azimuth. Along the axis of the counters, charge division on resistive wire allows the measurement of the position of hits with an experimentally determined σ of about 6 cm as shown in Fig. 30. This is comparable to the multiple scattering for the muons from ψ decays, 4 cm for the inner layer and 6.5 cm for the outer layer of the muon detector.

The tubes are 420 cm long which corresponds to 65% of the total solid angle. The tubes are arranged in groups of 8 with all the electronics at one end. At the other end, pairs of wires from non-contiguous tubes are connected together.

There are calibration inputs at both ends.

The electronics includes an addressable array of sample and hold circuits for pulse height measurement needed for Z determination by charge division. There are also pulsed outputs onto a 50 ohm line which are used in a cosmic ray veto and for checking high voltage plateaus. The typical electronic failure rate has been about 1/1000 per channel per month. However, since the wires are read out at both ends, these losses only cause a loss in Z information but not in muon identification.

The gas consists of 20% methane and 80% argon, and the counters are operated at 2700 volts. The efficiency of the counters has been measured to be 99% or better when the oxygen impurity is less than 150 parts per million. This is maintained by flowing the gas at a rate that produces a volume change every 36 hours.

We have used a sample of pions from the decay $\psi \rightarrow \rho\pi$ to measure the misidentification of pions as muons. The pions reach the muon counters if they do not interact sufficiently in the steel absorber (punch through) or if they decay in flight. For pions with momenta between 1.0 and 1.5 GeV/c, the fraction that reach the inner muon detection layer is about 14% while 4.5% reach the outer detection layer. The dependence on pion momentum is shown in Fig. 31.

The muon detection system has been very useful in providing an early sample of 85,000 muon pairs from ψ decays. These back to back dimuons have been used to check out and calibrate the other detection systems of Mark III. The angular distribution of these dimuons versus $\cos\theta$ is shown in Fig. 32; the solid line is $1 + \cos^2\theta$.

9. Trigger [8]

The event trigger is based on information from the drift chambers and from the time of flight counters. At SPEAR, the electron and positron bunches collide every 780 nsec which leads naturally to a trigger logic composed of several levels, each occupying the time between successive beam crossings. A decision made

prior to 590 ns after a collision will not result in any dead time, so it is important to have an efficient first level decision. The 590 ns limit is required to allow time to discharge capacitors used in sample and hold electronics. An event candidate which satisfies the first level is processed further, sacrificing one collision, and a second level decision is made. This trigger has three such levels. If an event fails at any level, the detector electronics is reset.

a. Level 1 Trigger

The level 1 trigger relies on the inner trigger chamber and time of flight counter information. The trigger simultaneously looks for two different event configurations called "two track" and "one track" events (up to 6 configurations are possible). If either trigger is satisfied the electronics are not reset and event processing continues at Level 2.

A "two track" trigger requires outputs from two trigger chronotrons (see section 4) and should only occur if at least two particles pass through the inner chamber. A "one track" trigger requires an output from one chronotron and a hit in one of the time of flight (ToF) counters. The ToF requirement reduces the background due to beam-gas scattering which generally produces a single, low transverse momentum electron which doesn't reach the ToF counters [9].

To obtain such time of flight information the output dynodes of the phototubes at both ends of each of the time of flight counters are run through chronotrons similar to those used with the inner chamber. This removes the time spread due to the position distribution of particles hitting the counters. The gate width of 27 ns suppresses cosmic rays by a factor of 29 in the one track trigger. The one track trigger covers 80% of 4π solid angle, while the two track trigger covers 88%.

In data taking at the $\psi(3097)$ energy region the level 1 trigger was satisfied at a 2 to 3 kHz rate while at the $\psi''(3770)$ it ran up to about 6 kHz, almost all of the rate being due to beam-gas scattering. Thus the trigger logic contributes a dead time of less than 0.4%.

b. Level 2 Trigger

In the level 2 trigger information from the main drift chamber is added to require rudimentary tracks in the drift chamber. Drift chamber layers 1,3, and 5 are used to find circular tracks originating at the beam line. To obtain a fast (25 ns) track selection each of the cells in layer 5 is put in coincidence with a swath of cells in layers 1 and 3 as shown in Fig. 33. Each cell in layer 5 is fed to a programmable array logic IC, along with the appropriate cells from layers 1 and 3. The logic arrays recognize triple coincidences of cells, corresponding to tracks having transverse momentum greater than a mimimum value, adjustable by the online computer to between 50 and 250 MeV. The one track trigger requires one such coincidence; the two track trigger requires two. Offline studies indicate an efficiency per track of 95.7% for transverse momenta above 70 MeV (using the 50 MeV cut). This includes the effect of drift chamber efficiency.

In running at the ψ with a luminosity of 4 x 10^{29}, a trigger rate from Level 2 of 3 Hz was obtained, 1.1 Hz from events occuring at the interaction vertex, 1.4 Hz from cosmic rays, and 0.5 from beam gas interactions. At the ψ'', where the luminosity is 2.5 $\times$ 10^{30}, the total event rate was 3.5 Hz, 0.25 Hz from real e^+e^- interactions, 1.5 Hz from cosmic rays, and 1.75 Hz from beam-gas.

In present operation, satisfaction of level 2 generates a computer interrupt causing the event to be written onto tape. The 30 ms needed to do this gives us a 10% dead time fraction for ψ'' running with the Level 2 trigger.

c. Level 3 Trigger

Backgrounds in running at the ψ and ψ'' have not been large enough to require a more stringent trigger selection. A third level can be put into effect which requires that tracks be approximately straight in Z and originate in the vertex region. The use of slower electronics for this requires about 100 μsec for a trigger decision at this level. Offline studies of the data indicate that the trigger rate could be reduced by a factor of 3 or 4 if level 3 were implemented.

10. Data Logging and Calibration

Readout of the pulse heights from the drift chamber, shower counters , and the ToF system, and event times from the drift chamber and ToF system is done by means of sample and hold circuits which are digitized by microprocessor controlled ADCs (Brilliant ADC's or BADC's Ref. [7]). At the time of electronics design there were no inexpensive IC's capable of accurate direct time to digital conversion. Data logging is done using a VAX 780 computer which is interfaced to the multiple BADC units.

Two types of calibration are done. The pedestals of all of the electronic circuit inputs to the BADC's are read about once every two hours and are stored on a disk to be loaded into the memory of the appropriate BADC unit for subtraction from the data before it is transmitted to the data logging computer. About once a day a calibration of all electronic systems is done by signals fed into the system inputs. For the drift chambers this involves varying the timing of signals which go to the discrimator circuits and checking the response of each channel in the system. Signals of varying amplitude are fed into the inputs of all amplifier circuits for both the drift chambers and the shower counters thus checking the amplifier linearity, the sample and hold circuits and the associated ADC's.

Quadratic coefficients are fitted from the response of each channel and stored on disk to be loaded in the appropriate BADC to allow the correction of the data before it is transmitted to the data logging computer.

Control of the calibration is done by one or more special modules associated with each subsystem and a single module which synchronizes them to the trigger system and allows the calibration of multiple subsystems simultaneously.

11. Luminosity Monitor

The luminosity monitor consists of defining counters and shower counters placed above and below the beam pipe just outside the compensating magnets at each end of the spectrometer 2.2 m from the interaction region as shown in Fig. 34. The defining counters are of scintillator 1.6 cm high, 5.7 cm wide, and

0.35 cm thick, starting 5.5 cm above or below the beam line (an angle of 25 milliradians to the beam direction). The shower counters placed behind them consist of 9 layers of 0.9 radiation length tungsten interleaved with scintillator.

Small angle Bhabha scattered electron-positron pairs must be counted in a large background of gas scattered particles. A Bhabha scattered pair is defined, for example, as a hit in the south-upper defining counter accompanied by a shower in its shower counter plus a shower in the north-lower counter. This is combined in an "Or" circuit with the south-lower north-upper output. Similarly the signals using the north-upper and north-lower defining counters in combination with south-lower and south-upper shower counters are recorded and added (not "Or'd") to the previous combination. The two defining counters in front of the two shower counters are not used in coincidence, as this would make the system more sensitive to beam spread and position.

The occasionally large beam gas scattering signal does not produce a coincidence and the intensity of accidentals is measured by delaying signals until the next beam crossing and making coincidences with false signals. This random coincidence signal number is then subtracted from the coincidence signal number to give a number proportional to the luminosity.

The relatively large horizontal width of the counters make them insensitive to the horizontal beam position if the counters are properly aligned. For vertical and longitudinal vertex displacements the smaller angle presented by one defining counter is compensated by the larger angle of its colinear opposite defining counter so that the sum of coincidences remains relatively insensitive to displacements if the counter separations are constant. A 3 mm displacement horizontally causes a 0.3% change while a 3 mm vertical displacement causes a 2% change. Longitudinal displacements can be large due to beam spread and here a displacement of the beam interaction half width, 10 cm, causes a 0.2% change.

The system was plateaued by placing the appropriate pairs of beam defining and shower counters in effective coincidence varying the voltage on one counter at a time while keeping the others constant.

The luminosity monitor is used as a relative monitor. The true luminosity is found by a study of larger angle Bhabha scattered e^+e^- pairs measured in the spectrometer. The two differ by about 10%.

12. System Performance

The checkout of the system was performed by taking data at the $\psi(3097)$ since the crossection and the event rate is largest at this resonance. The results reported come from a period of data taking at this energy during which 2.7 million ψ decays were observed.

The data analysis concentrates on the investigation of hadronic and electromagnetic decays requiring that all final state particles be detected. After selecting event topologies, the events are kinematically fitted to a decay hypothesis with the requirement of energy and momentum conservation. Then further cuts are applied to reduce background and allow the extraction of the signal from the channel under investigation.

Figures 35 through 39 show one event displays. In Fig. 35, which shows a muon pair, hits can be observed in all components of the spectrometer including, at the perimeter, both sets of muon counters.

Figure 36 shows the response of the detector to a Bhabha scattered e^+e^- pair. Shower development typical of that for electrons and photons can be observed in the shower counter.

Time of flight information is important for the investigation of final states with kaons or protons. In Fig. 37 a view is shown of the interaction $\psi \rightarrow \gamma\phi\phi$. All kaons are identified by time of flight.

Figure 38 shows an event with 5 photons and 4 pions. The ability of the detector to handle such events is shown in Figs. 39 (a) and (b). After isolation of π^o candidates, a plot is made of the $\pi^+\pi^-\pi^o$ mass in Fig. 39 (a) where an ω peak is clearly visible. Selecting events with an ω the other $\pi^+\pi^-\pi^o$ combinations are plotted in Fig. 39(b) revealing a second ω and thus the reaction $\psi \rightarrow \gamma\omega\omega$.

Plots of $\eta\pi\pi$ mass from $\psi \rightarrow 3\gamma\pi\pi$ show an $\eta\prime$ signal for a 4C fit in Fig. 40 and a 5C fit in Fig. 41.

The good low energy photon efficiency is possibly best illustrated by measurements of the reaction $\psi \rightarrow \pi^+\pi^-\pi^o$. In Fig. 42 a Dalitz plot of the Mass^2 of $\pi^+\pi^o$ vs. Mass^2 of $\pi^-\pi^o$ shows complete domination by ρ final states and a quite uniform filling of the plot in the low mass square corner occupied by low energy π^os.

Acknowledgements

We wish to thank members of the Mark II and HRS collaborations for advice during the design of the Mark III. The SLAC rigging group provided accurate and delicate handling of the heavy equipment during assembly and installation, while the Linear Accelerator and SPEAR operators provided excellent beams for our debugging and data-taking.

REFERENCES

[1] S. Neddermeyer et al., Rev. Sci. Inst. 18 (1947) 488.

[2] J. Roehrig et al., SLAC-PUB-3199, Submitted to NIM.

[3] J. S. Brown et al., SLAC-PUB-3180, Submitted to NIM.

[4] J. E. Grund, SLAC-PUB-2416 (Oct. 1979).

[5] K. Bunnell et al., SLAC-PUB-3140, Submitted to NIM.

[6] R. Fabrizio et al., SLAC-PUB-3200.

[7] M. Breidenbach et al., SLAC-PUB-2032 (Oct. 1977), IEEE Trans. Nucl. Sci. NS-25, No.1 (1978) 706-710.

[8] J. Thaler et al., IEEE Trans. Nucl. Sci. NS-30 (1982) 236.

[9] A. Seiden et al., Nucl. Instrum. Methods 193 (1982) 597.

Table 1

Material Thicknesses Traversed by Particles

Beam pipe (15 cm diam., 1.5 mm thick Be)	0.0040 r.l.
Inner Trigger Chamber	0.0068 r.l.
Inner wall of Drift Chamber	0.0016 r.l.
Drift Chamber gas	0.0075 r.l.
Drift Chamber wires	0.0015 r.l.
Total material	0.0214 r.l.

Table 2

Drift Chamber Specifications

Inner radius	14.47 cm
Outer radius	114.26 cm
Layer 2	
Length	177.8 cm. 32 cells
Number of wires per Cell	15
Innermost wire #1	17.45 cm radius
Outermost wire #15	31.45 cm radius
Charge division wires #1 & #15	57μ diam. s.s.
Sense wires #2-14	20μm diam. tungsten
Smallest half width (at wire #2)	1.81 cm 400 ns
Largest half width (at wire #14)	2.99 cm 660 ns
Displacement of alternate sense wires	$\pm$ 150 μm
Layers 3 - 8	
Length	233.7 cm
Number of wires per cell	5
Wires #1 and #5, guard and charge division	57 μm diam. s.s.
Wires #2, #3, and #4, sense wires	20 μm tungsten
Field wires	175 μm BeCu
Radius of center wire #3	13.45 x N cm (N = layer number)
Number of cells	16 $\times$ N
Angle of stereo layer 4	7.7 degrees
Angle of stereo layer 6	-9.0 degrees
Charge division	layers 3,5, and 7
Half cell width	2.64 cm $\approx$580 ns
Staggering	$\pm$400 μm

Table 3

Barrel Shower Counter Specifications

Spool length	385.0 cm
Spool outer diameter	252 cm
Spool thickness	2.3 $\pm$0.4 cm
Flange outer diameter	261.8 cm
Cell width, inner layer	2.4 cm
Cell width, outer layer	3.2 cm
Gas thickness per cell	1.27 cm
Length of active volume (including anterior ribs)	348.00 cm
Number of layers	24
Thickness of aluminum sheets	0.064 cm
Thickness of lead sheets	0.28 cm
Thickness of Al, Pb, Al glue sandwich	0.46 cm
Length of Pb sheets	348.00 cm
Number of Pb sheets per circumference	10
Width of ribs	2.67 cm
Height of I-beams	1.24 cm
Width of top flange of I-beams	1.02 cm
Thickness of I-beam material	0.076 cm
Sense wire type	Stablohm 800 s.s.
Sense wire diameter	46 μm
Gas	80% argon; 20% methane
Gas flow	10000 liters (one volume) per day

Table 4

Endcap Shower Counter specifications

Distance from interaction regions	
Front layer	139.0 cm
Back layer	177.8 cm
Radius of sensitive regions	
Outer	105.4 cm
Inner	35.0 cm approx.
Radius of assemblies	
Outer	110.5 cm
Inner	32.5 cm
Polar angle of sensitive region	
Front outer	37.2 degrees
Front inner	14.1 degrees
Back outer	31.9 degrees
Back inner	11.1 degrees
Solid angle subtended	
Front	$2 \times 8.5\% \times 4\pi$
Back	$2 \times 6.5\% \times 4\pi$
Tube thickness, interior	1.17 cm
Tube width, interior	2.71 cm
Tube wall thickness	0.064 cm
Lead thickness per layer	0.279 cm
Adhesive thickness per layer	0.025 cm
Number of layers	24
Number of cells per layer	94
Sense wire type	Stablohm 800 s.s.
Sense wire diameter	37 μm
Gas type	80% argon, 20% methane
Gas flow	1 volume per day

Table 5

Muon Detection System

135 Modules of 8 tubes; 1/3 overlap of adjacent tubes	
Tube size	5 cm outer diameter, 4.2 m long
Wire size	50 μm s.s. 380 Ω/m for charge division
Gas	80% argon, 20% methane, 100 ppm O_2
Gas flow	1 vol. change per 36 hours
Absorber for inner layer	coil, shower counter, & 20 cm iron
Absorber for outer layer	an additional 13 cm of iron
Multiple scattering for 1 GeV/c muons	
Inner layer	5 cm equivalent
Outer layer	9 cm equivalent
Calibration	Charge injection directly on wires
Resolution in azimuth	1 cm (4 mr)
Resolution axially	6 cm (24 mr)

FIGURE CAPTIONS

1. End view of Mark III Spectrometer.
2. Side view of Mark III Spectrometer.
3. (a). End view of the Inner Trigger Chamber.

   (b). End view showing the offset of layers of the Inner Trigger Chamber.
4. Chronotron resolution for reconstructed hadrons. T1 and T2 are the times for layers 1 and 2 of the Inner Trigger Chamber.
5. Side view of the Drift Chamber.
6. End view of a section of the Drift Chamber.
7. Schematic for the electronics for Layer 2 of the Drift Chamber.
8. Schematic for the electronics for Layers 3-8 of the Drift Chamber.
9. Time differences for offset wires of Layer 3 of the Drift Chamber showing the resolution of the left-right ambiguity.
10. Efficiencies of cells in Layer 3 of the Drift Chamber. Two of the three wires in a cell are required to have a signal.
11. Residuals of fitted Tracks for Layer 5 in the Drift Chamber. Layer 5 is left out of the fit and the plotted quantity is the predicted position minus that measured.
12. Measured momenta for muons produced from ψ decay. The superimposed curve has a σ of 45 MeV/c.
13. Azimuthal accuracy of the Drift Chamber. The predicted ϕ angle of one member of a muon pair from ψ decay minus its measured angle.
14. λ accuracy of the Drift Chamber. The predicted λ angle of one member of a muon pair from ψ decay minus its measured angle.
15. dE/dx measurements on low energy particles. K and π bands are visible.

16. Scintillation counters and light pipes mounted on the exterior of the Drift Chamber.

17. Differences between predicted and measured times for Bhabha Scattered electrons ($\sigma = 171$ psec).

18. Scatter Plot of β vs momentum showing e,π, K, and p bands.

19. Barrel Shower Counter.

20. End Cap Shower Counter.

21. Schematic of shower counter electronics.

22. Energy deposited in the shower counter by Bhabha Scattered electron-positron pairs as a function of longitudinal position.

23. ϕ resolution of the Barrel Shower Counter.

24. Z resolution of the Barrel Shower Counter.

25. (a) and (b). Energy linearity of the Barrel Shower Counter.

26. Energy resolution of the Barrel Shower Counter.

27. Detection efficiency of the Barrel Shower Counter. The points plotted show the photon energy distribution from $\psi \rightarrow \rho^o\pi^o$ which produces a flat energy distribution of photons. The 100% normalization for efficiency is derived from other measurements in which the energy of a photon is kinematically predicted from the same interaction.

28. Mass of 2 γ combinations from $\psi \rightarrow \gamma\gamma\gamma\pi^+\pi^-$. The π^o and η are clearly seen.

29. Tube arrangement of the muon tube module.

30. Difference of Z determination of overlapping muon tubes from charge division.

31. The fraction of pions or their decay products which reach the muon detector. The upper data are for the inner layer and the lower data are for the outer layer.

32. θ distribution of dimuon pairs.

33. Circle fit track finding schematic.

34. Luminosity Monitor arrangement.

35. Muon pair.

36. Bhabha Scattered e^+e^- pair.

37. $\psi \rightarrow \gamma\phi^+\phi^-$.

38. $\psi \rightarrow 5\gamma\pi^+\pi^-\pi^+\pi^-$.

39. (a). $\pi^+\pi^-\pi^o$ mass from $\psi \rightarrow 5\gamma\pi^+\pi^-\pi^+\pi^-$ with ω clearly visible.

    (b). $\pi^+\pi^-\pi^o$ mass recoiling from a $\pi^+\pi^-\pi^o$ combination in the ω region of Fig. 12.5 a.

40. $\eta\pi^+\pi^-$ mass from $\psi \rightarrow \gamma\gamma\gamma\pi^+\pi^-$. γ pair masses are selected from the η region and a 4c fit made.

41. $\eta\pi\pi$ Mass from $\psi \rightarrow \gamma\gamma\gamma\pi^+\pi^-$. After selection of events with γ pair masses in the η region a 5c fit is made assigning the η mass to the γ pair.

42. Dalitz Plot of Mass^2 $\pi^+\pi^o$ vs Mass$^2\pi^-\pi^o$

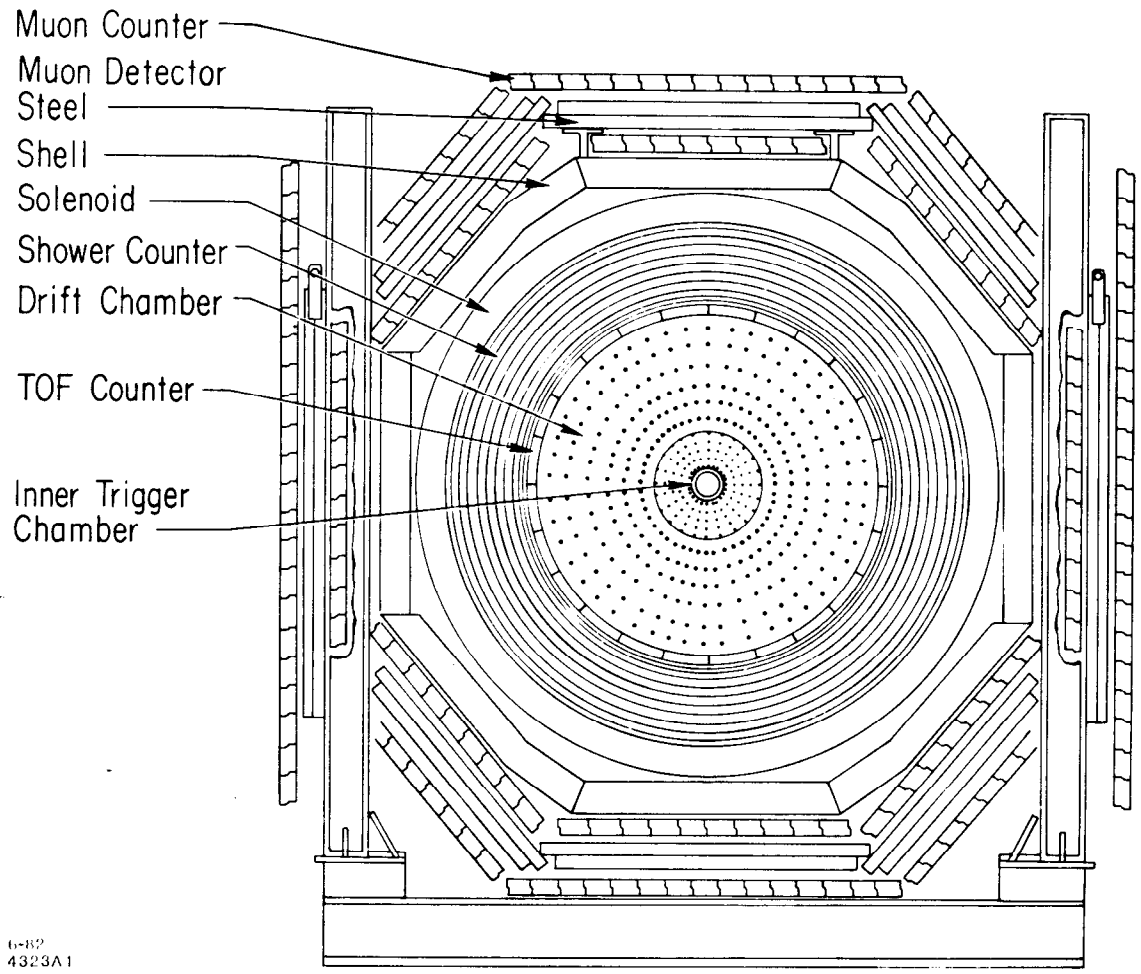
Muon Counter
Muon Detector
Steel
Shell
Solenoid
Shower Counter
Drift Chamber
TOF Counter
Inner Trigger
Chamber
6-82
4323A1

Fig. 1

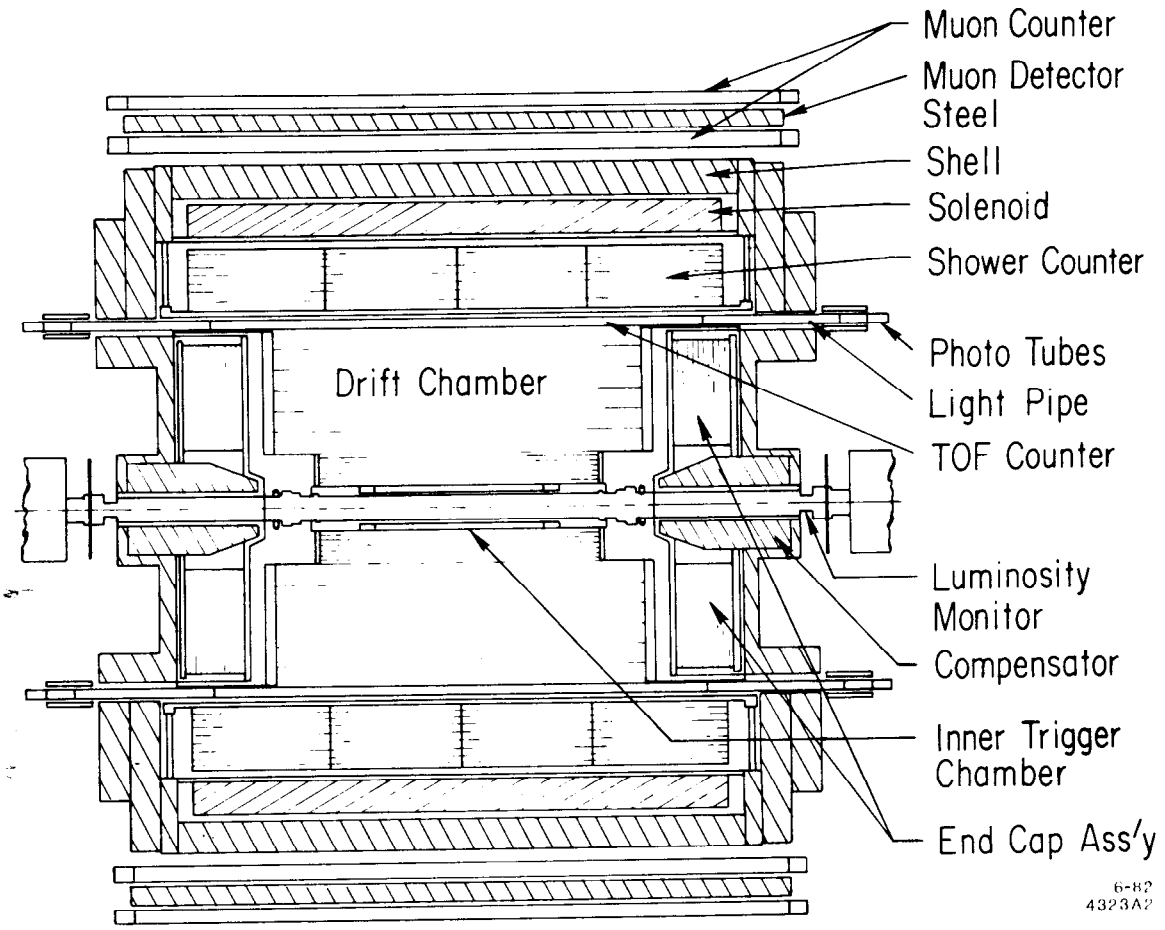
Muon Counter
Muon Detector Steel
Shell
Solenoid
Shower Counter
Photo Tubes
Light Pipe
TOF Counter
Drift Chamber
Luminosity Monitor
Compensator
Inner Trigger Chamber
End Cap Ass'y
6-82
4323A2

Fig. 2

(a)

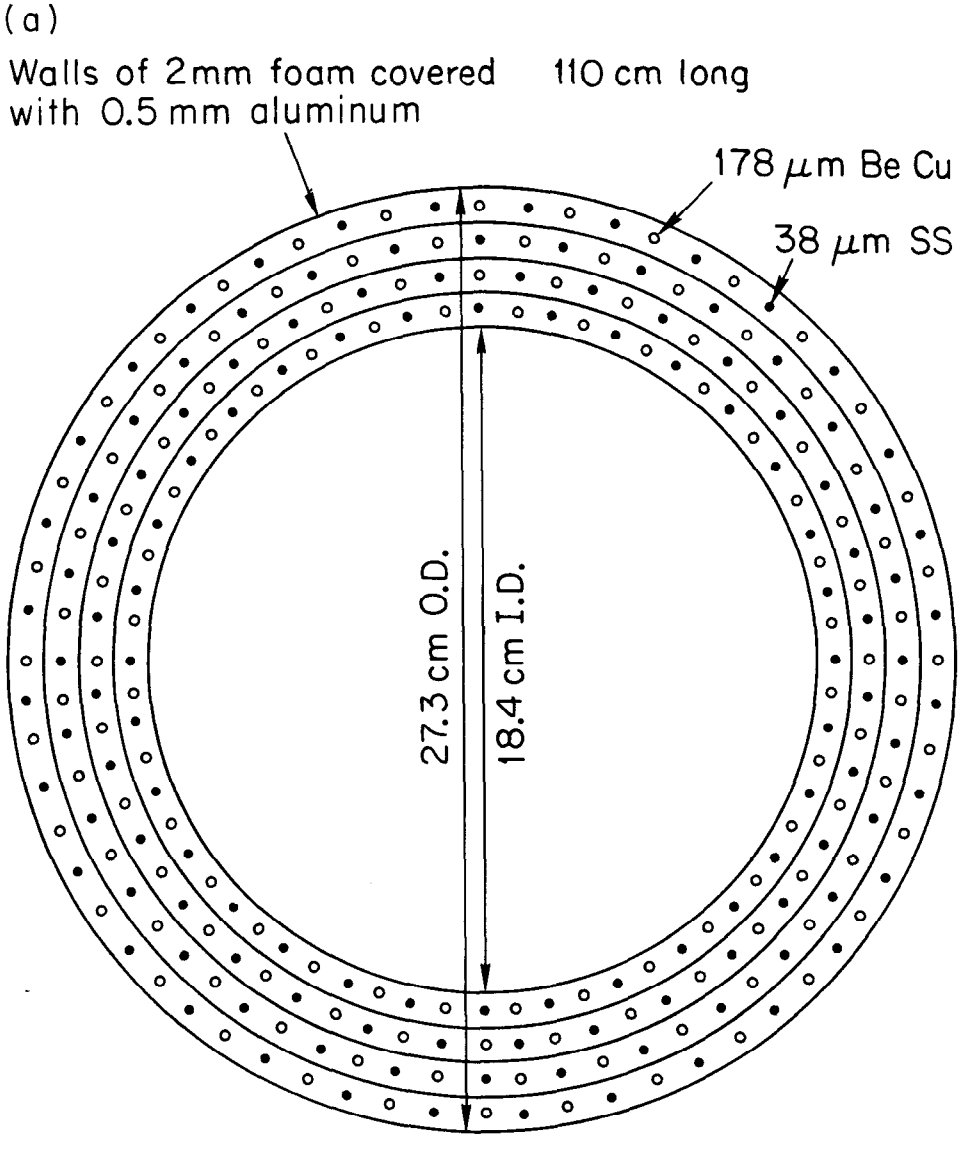

(b)

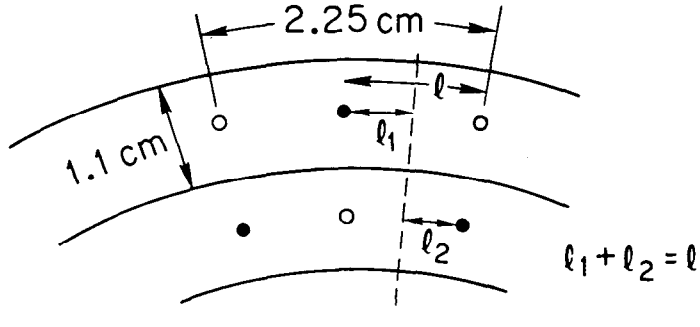

6-83
4569B4

Fig. 3

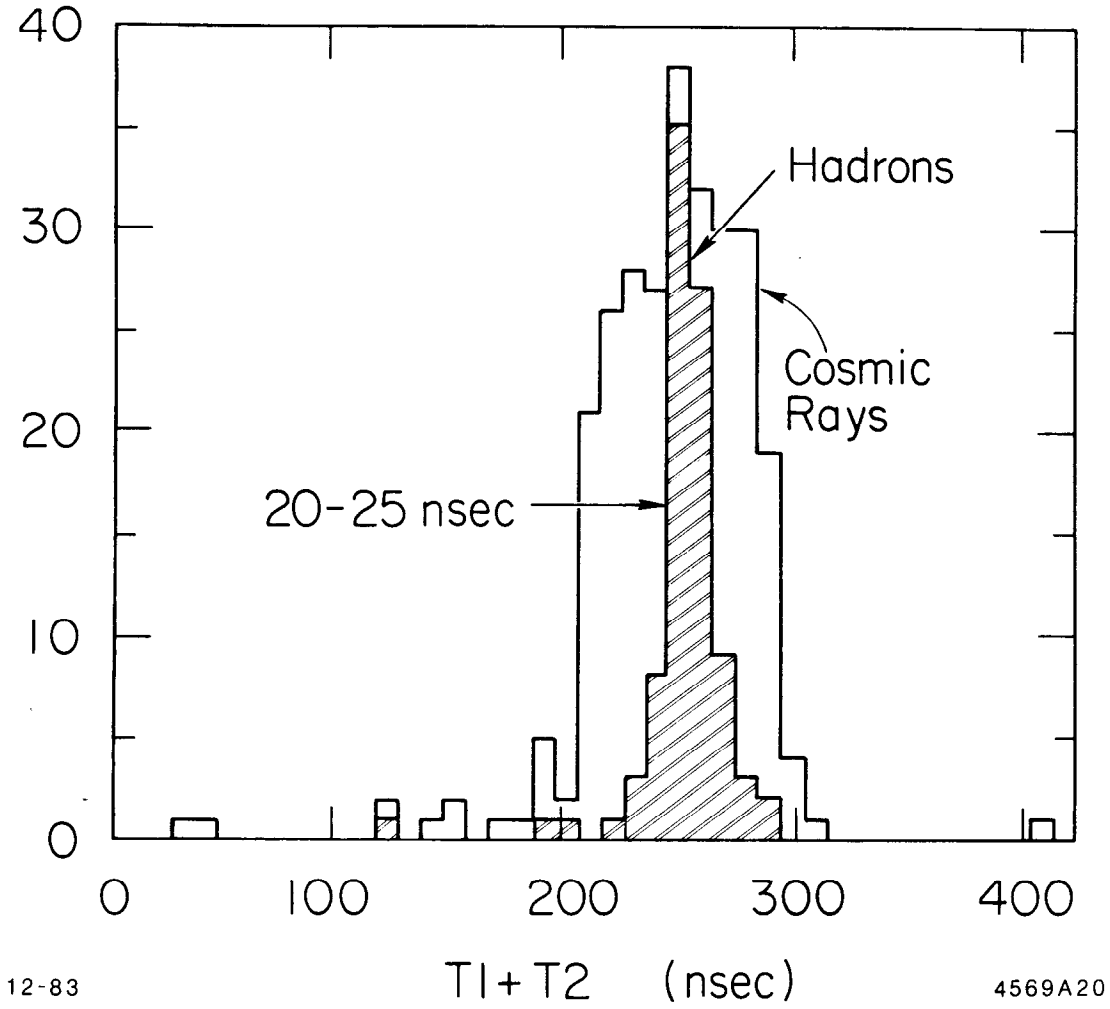
40
30
20
10
0
0
100
200
300
400
Hadrons
Cosmic
Rays
20-25 nsec
T1+T2 (nsec)
12-83
4569A20

Fig. 4

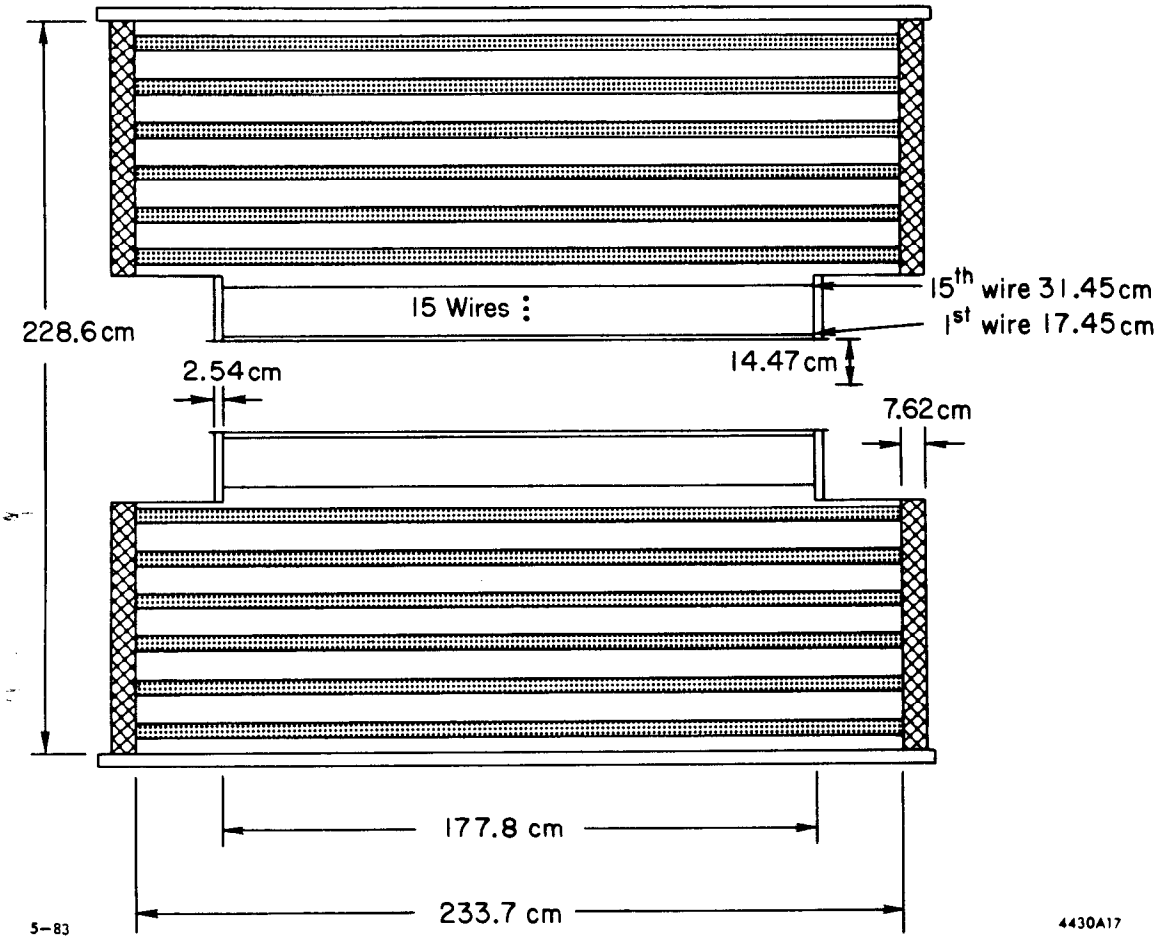
228.6 cm
15 Wires
15th wire 31.45 cm
1st wire 17.45 cm
14.47 cm
2.54 cm
7.62 cm
177.8 cm
233.7 cm
5-83
4430A17

Fig. 5

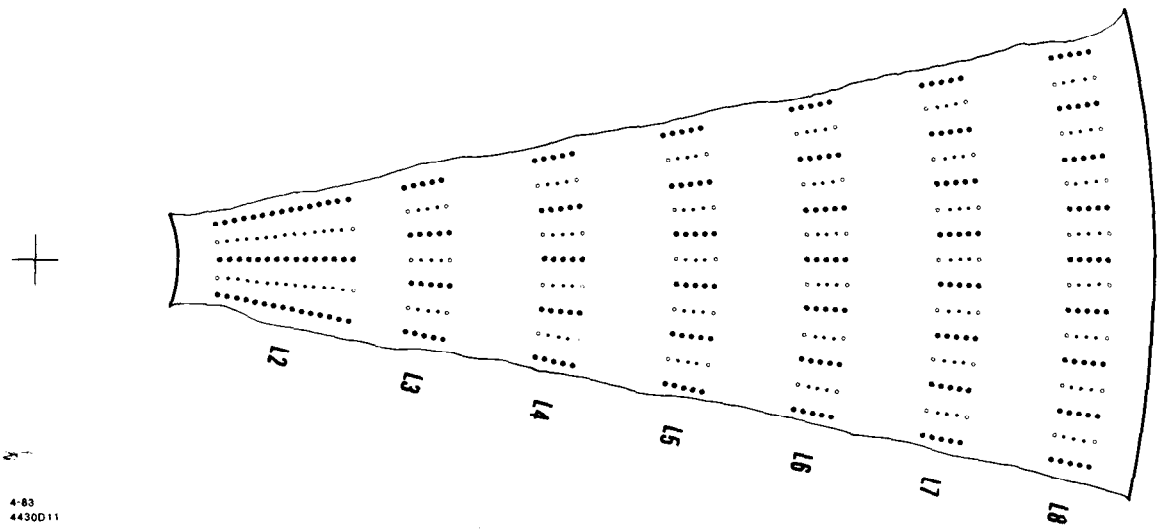

4-83
4430D11

Fig. 6

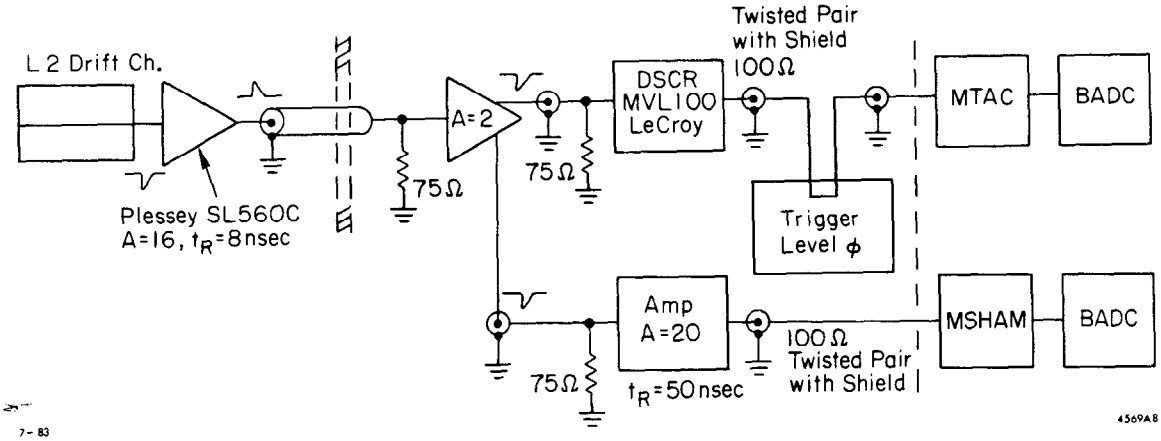
L 2 Drift Ch.
Plessey SL560C
A=16, t_R=8nsec
75Ω
A=2
75Ω
DSCR
MVL100
LeCroy
Twisted Pair
with Shield
100Ω
Trigger
Level ϕ
MTAC
BADC
Amp
A=20
75Ω
t_R=50nsec
100Ω
Twisted Pair
with Shield
MSHAM
BADC
7-83
4569A8

Fig. 7

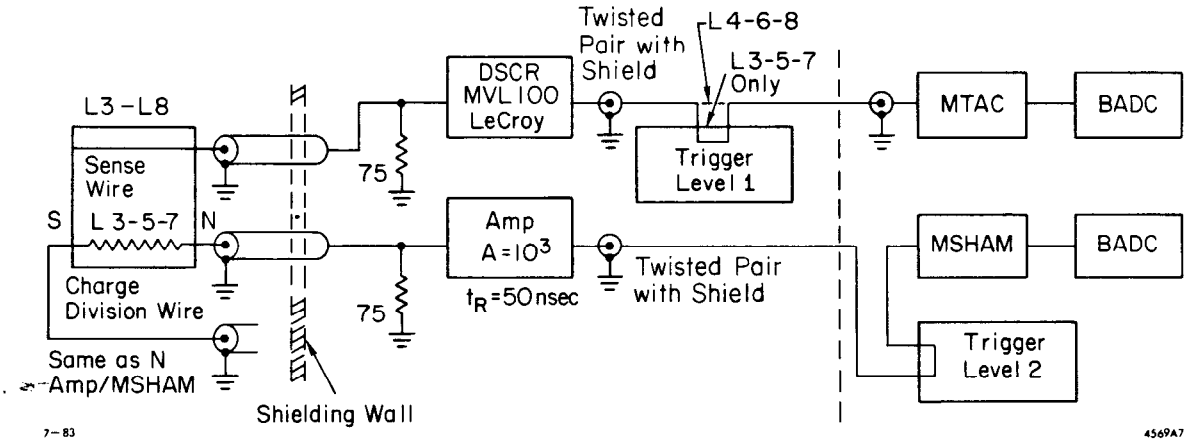
Twisted
Pair with
Shield
L4-6-8
L3-5-7
Only
DSCR
MVL100
LeCroy
MTAC
BADC
L3-L8
Sense
Wire
75
Trigger
Level 1
S
L3-5-7
N
Amp
A=10³
MSHAM
BADC
Charge
Division Wire
75
t_R=50nsec
Twisted Pair
with Shield
Trigger
Level 2
Same as N
Amp/MSHAM
Shielding Wall
7-83
4569A7

Fig. 8

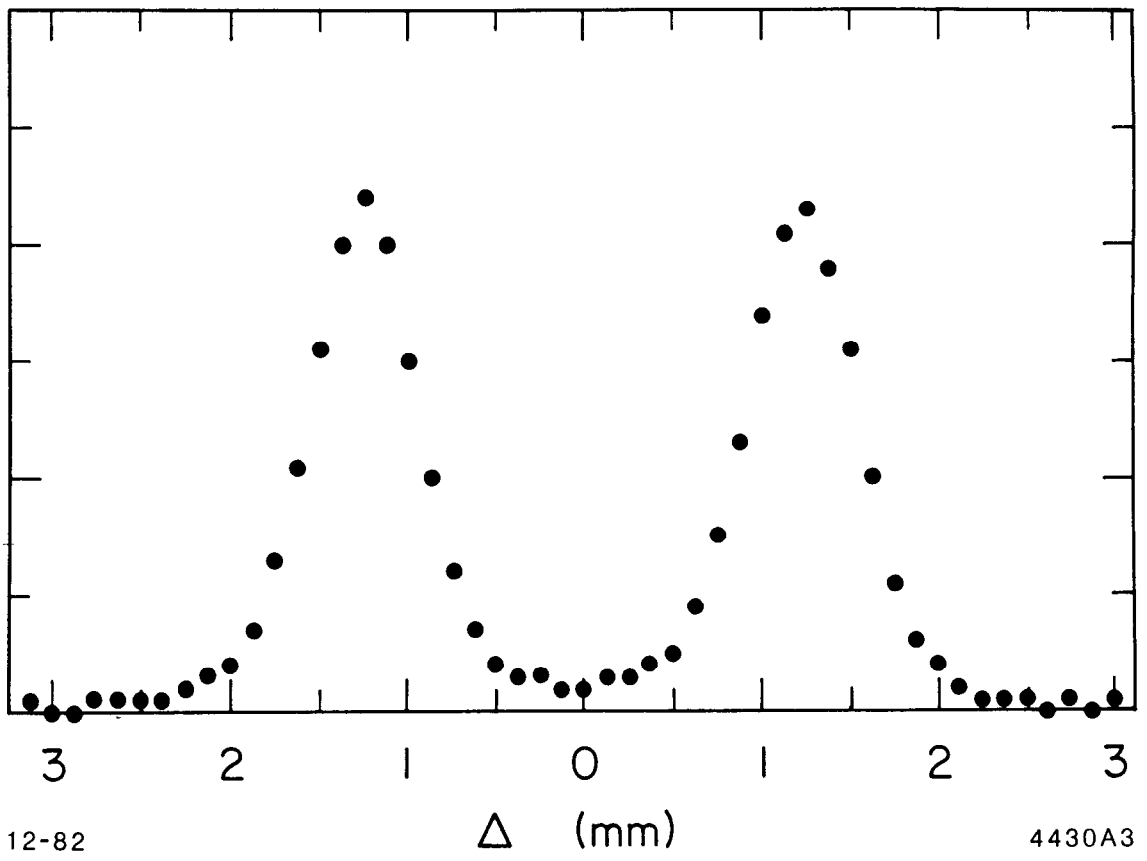

Fig. 9

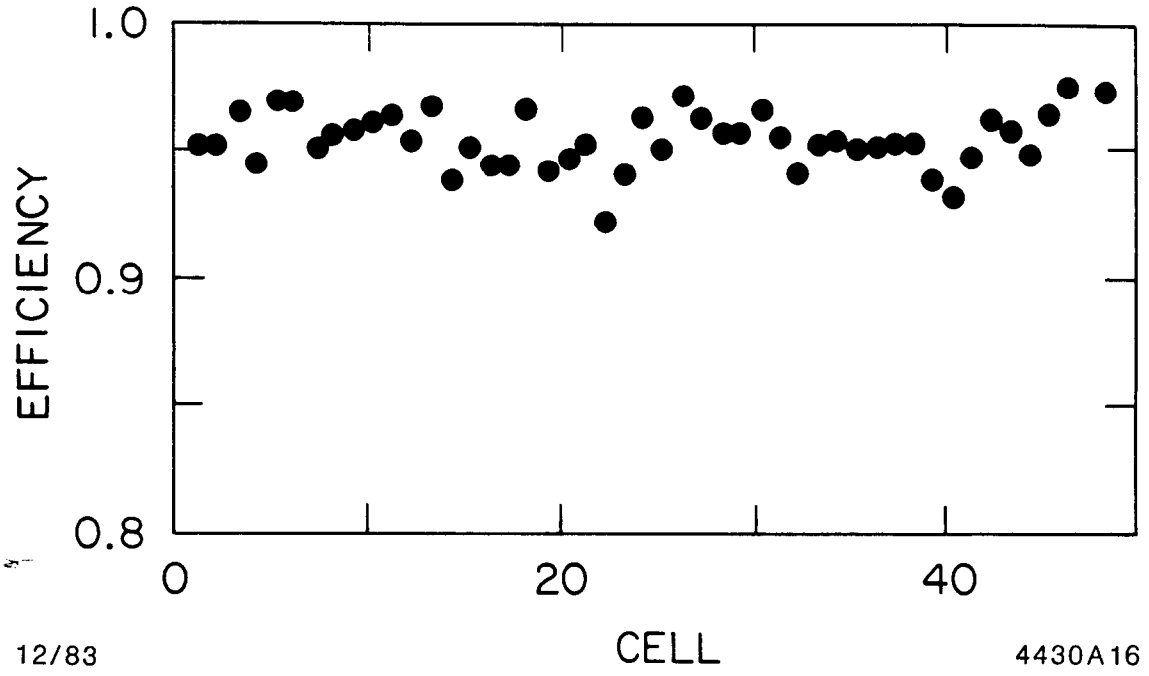

Fig. 10

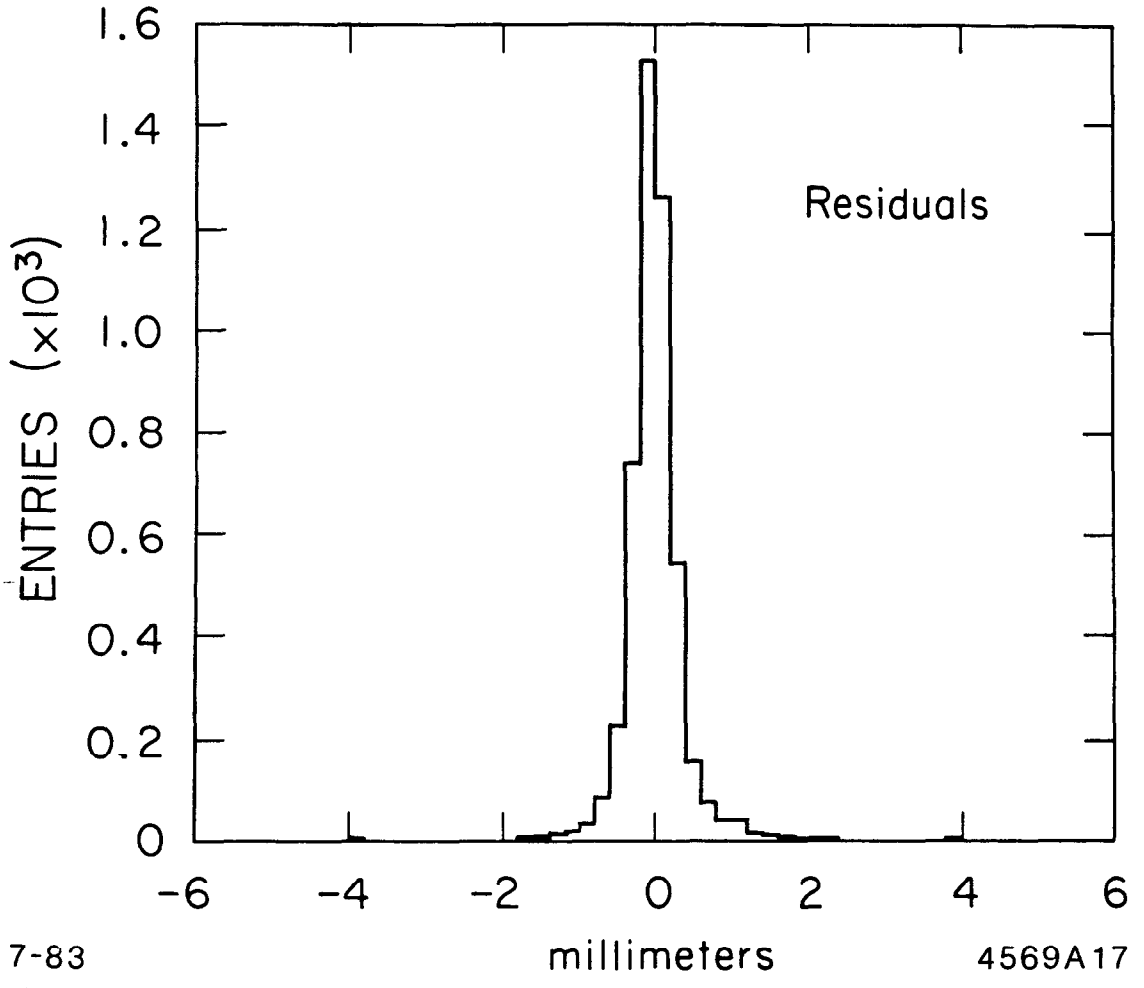
1.6
1.4
1.2
1.0
0.8
0.6
0.4
0.2
0
ENTRIES (x10³)
Residuals
-6
-4
-2
0
2
4
6
millimeters
7-83
4569A17

Fig. 11

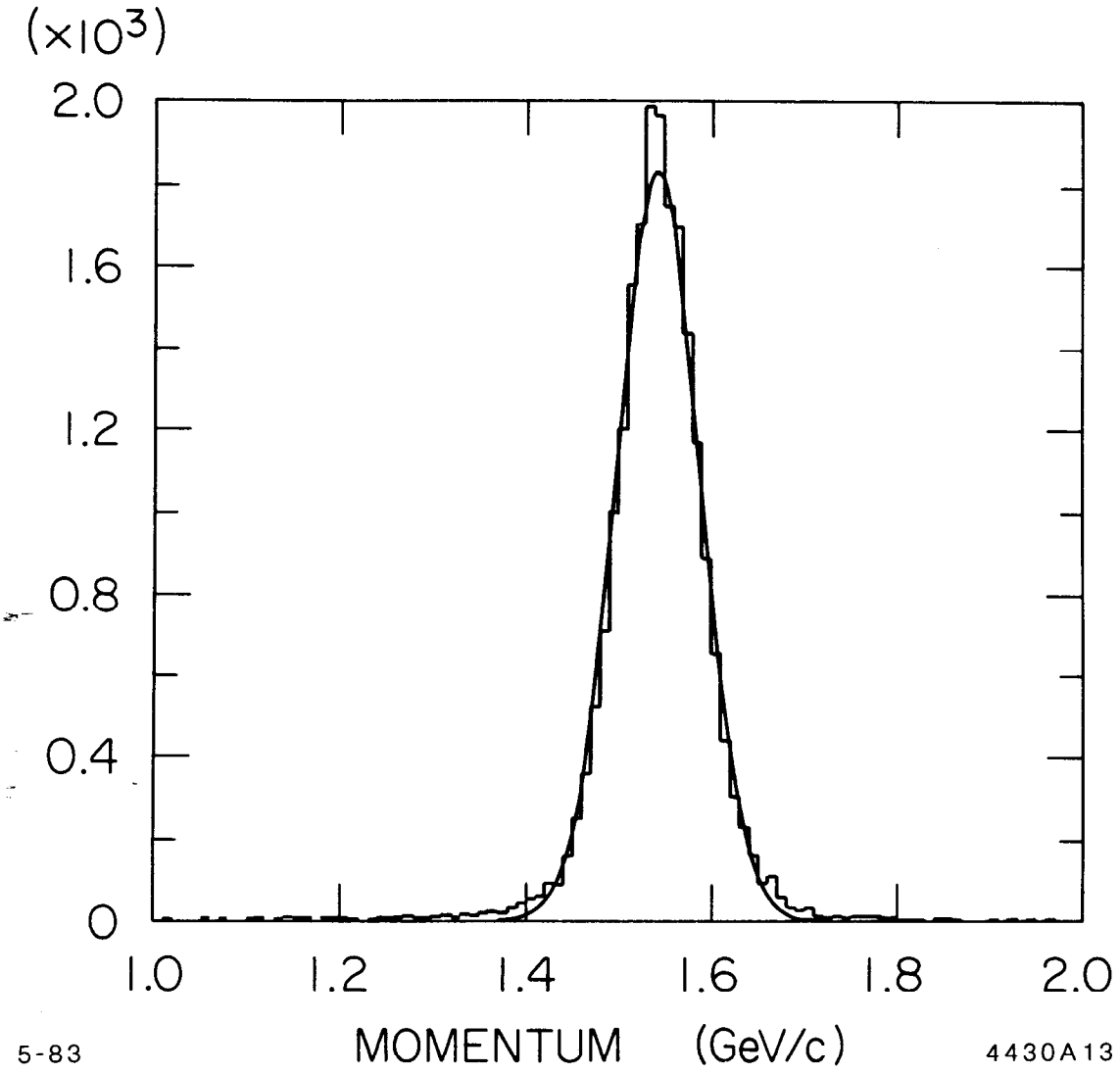

Fig. 12

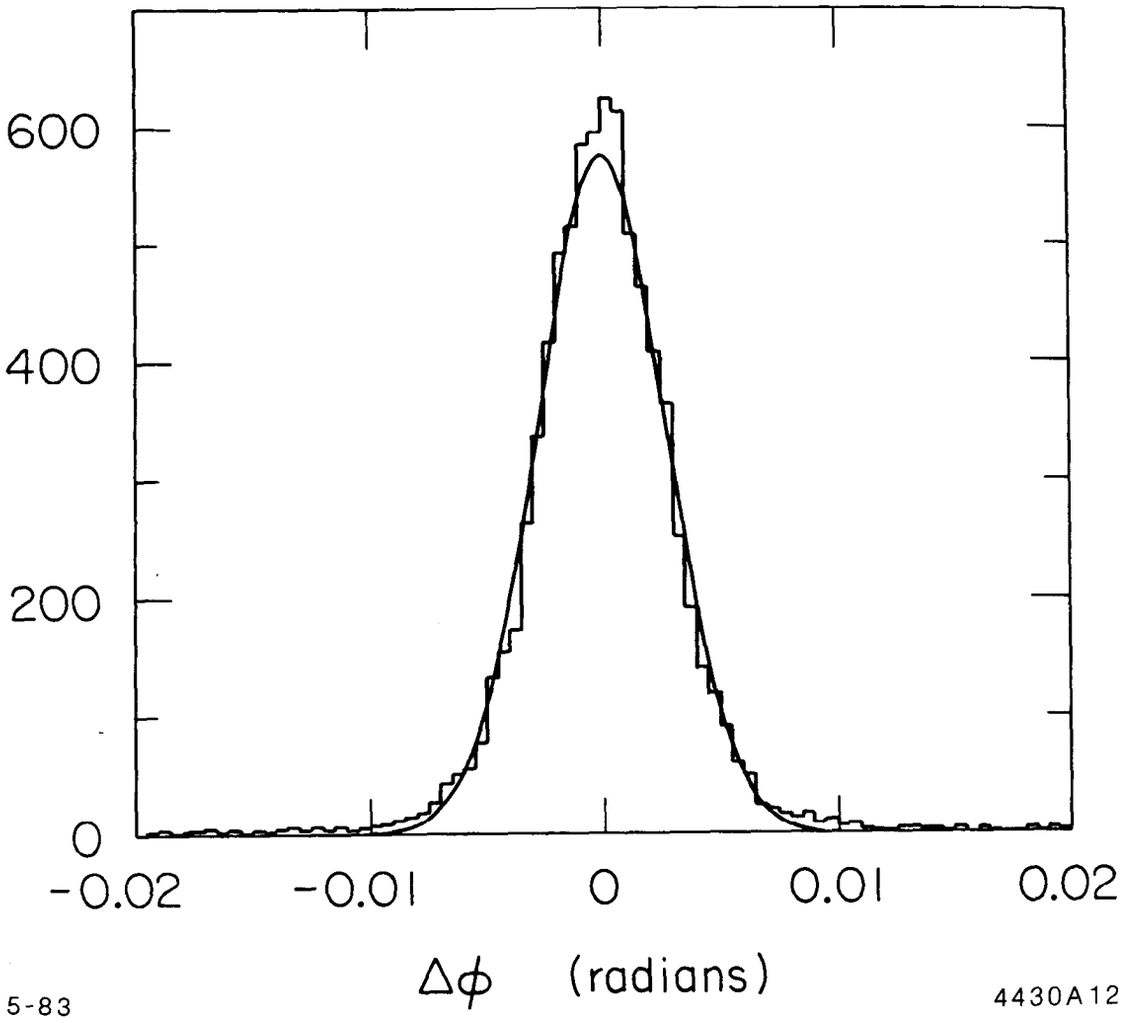

Fig. 13

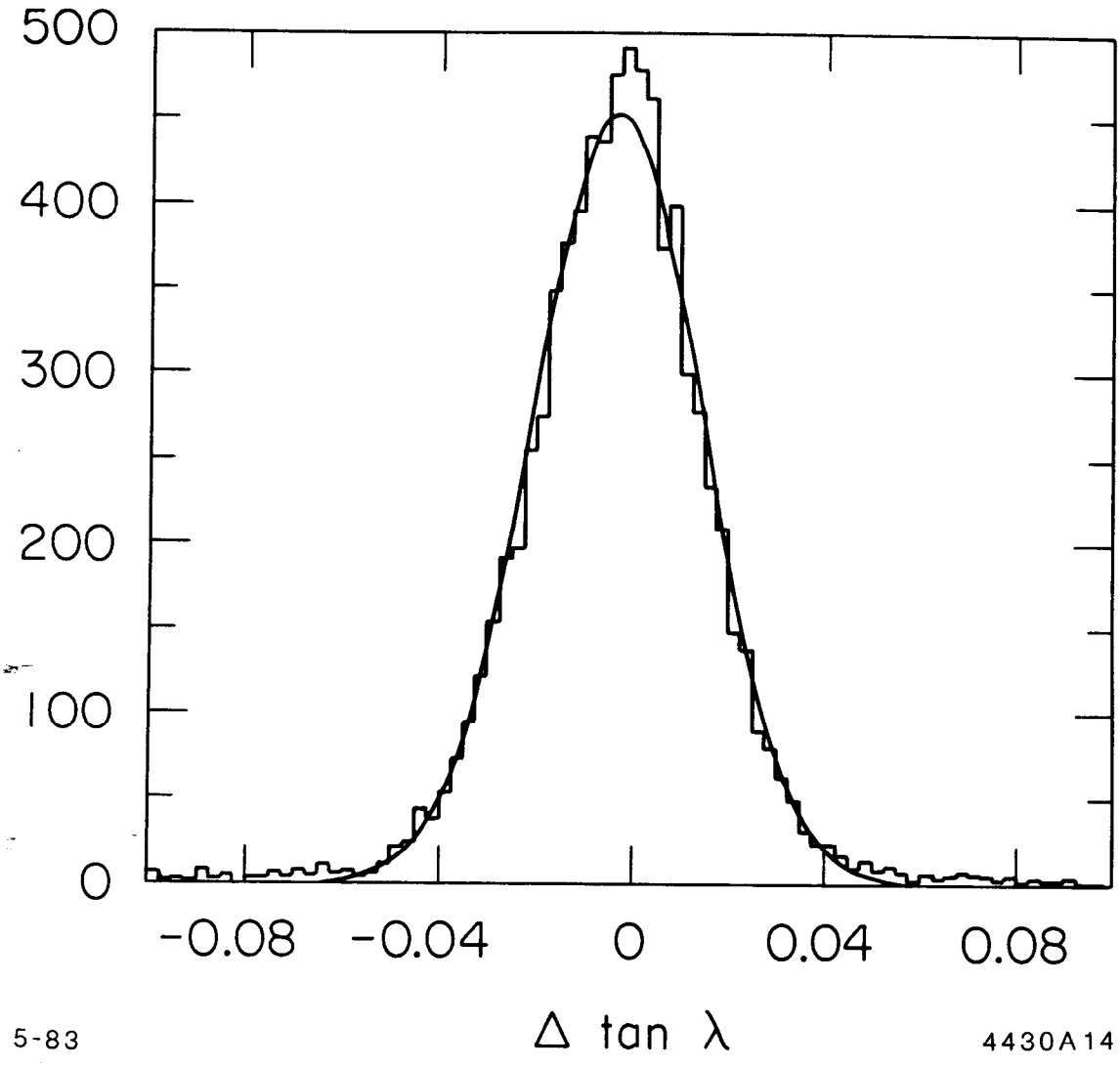

Fig. 14

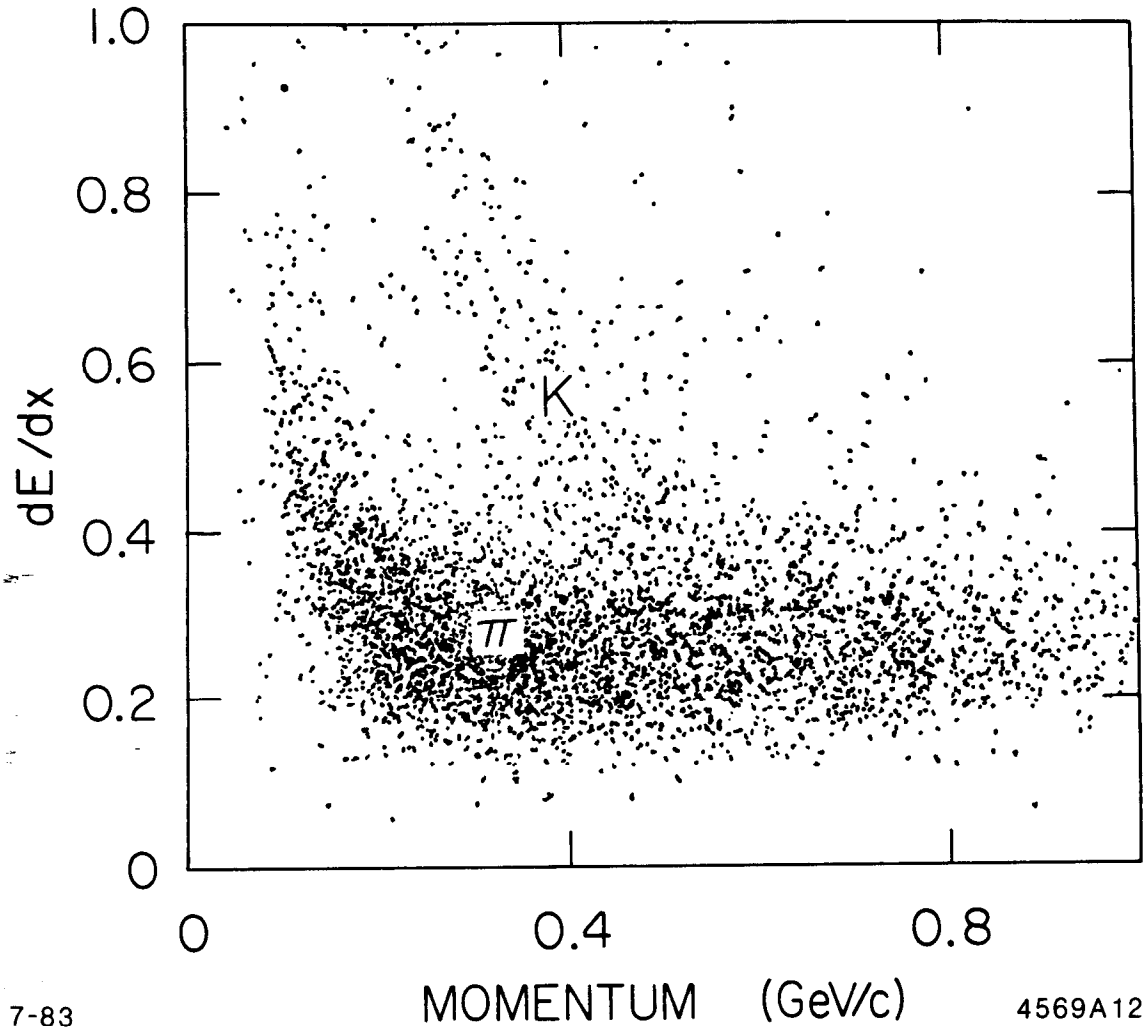

Fig. 15

MARK III TIME OF FLIGHT

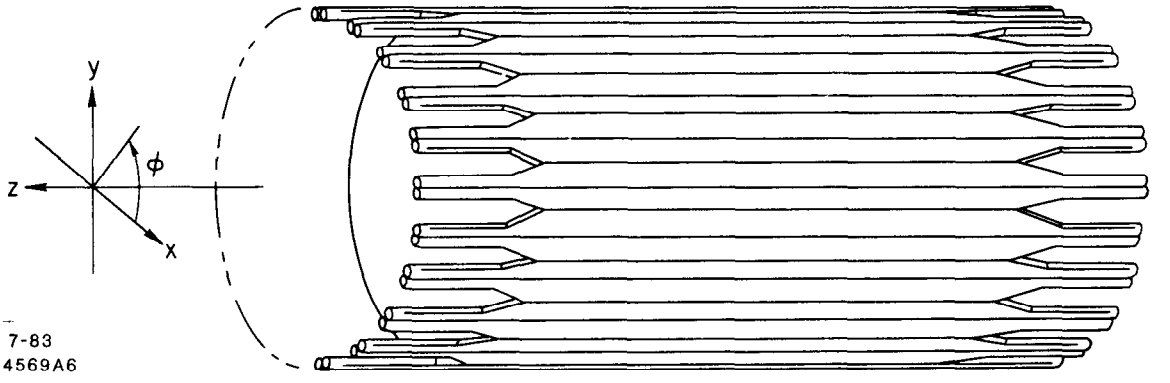

Fig. 16

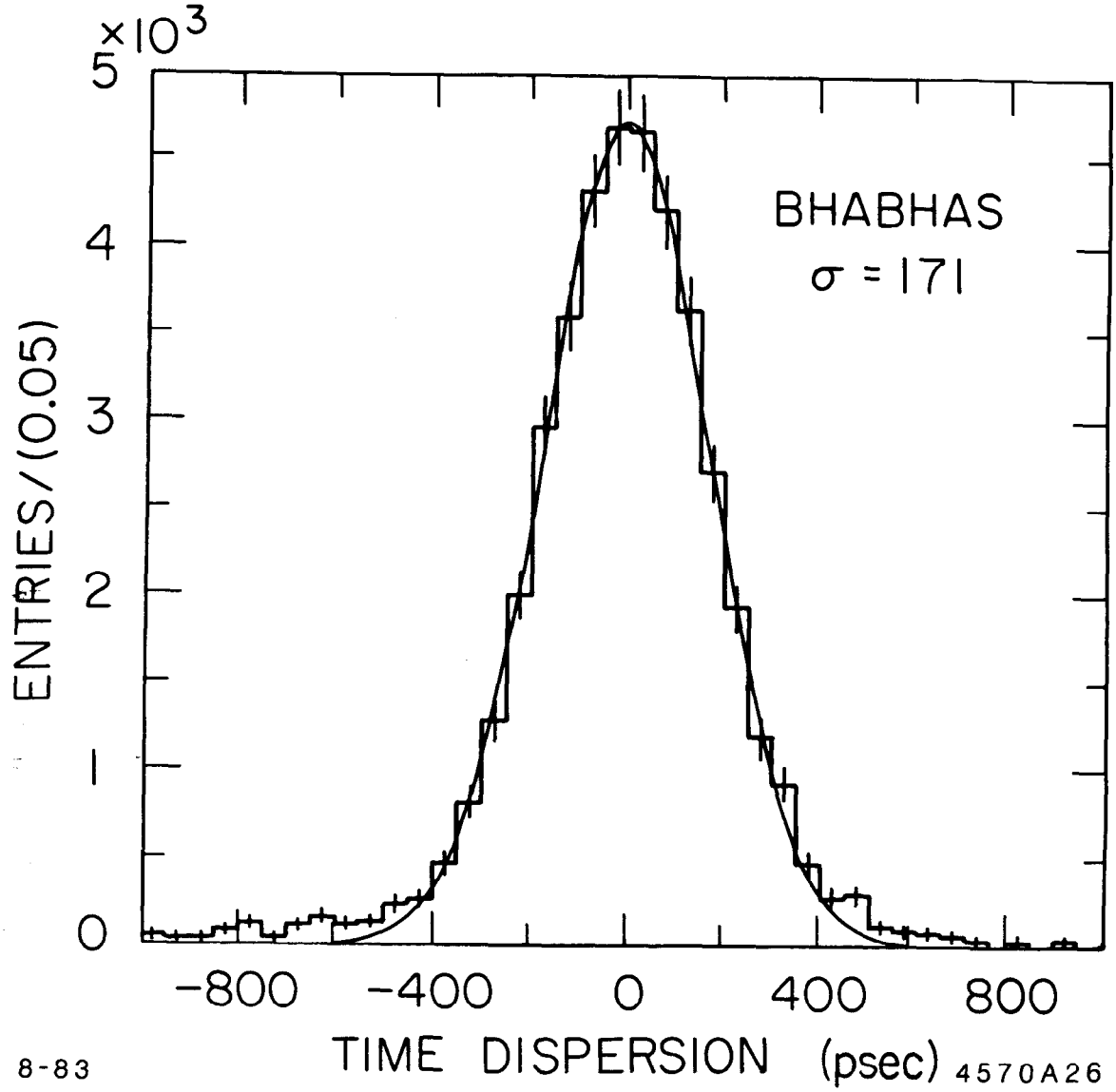
x10^3
5
4
3
2
1
0
ENTRIES/(0.05)
BHABHAS
σ = 171
-800
-400
0
400
800
TIME DISPERSION (psec)
8-83
4570A26

Fig. 17

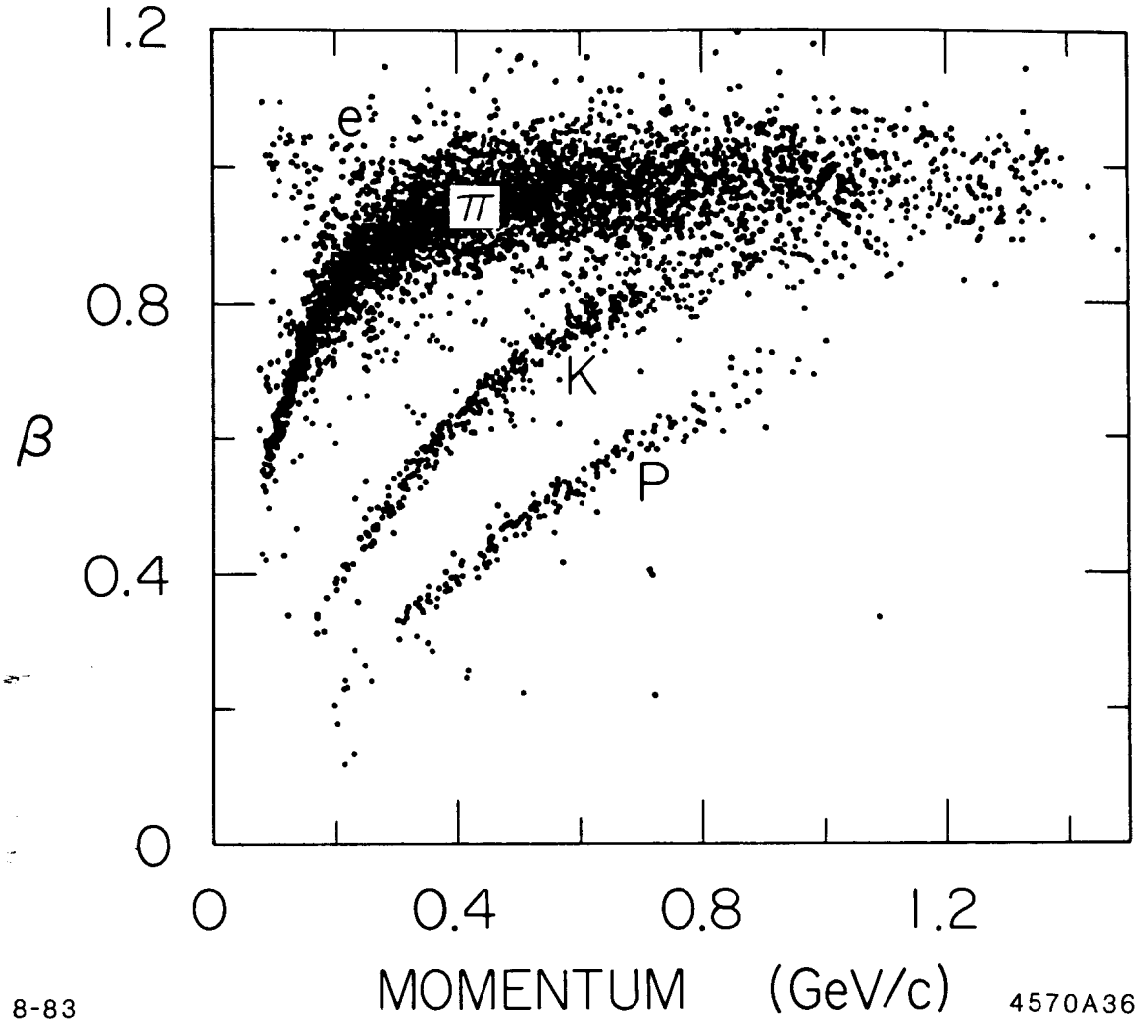

Fig. 18

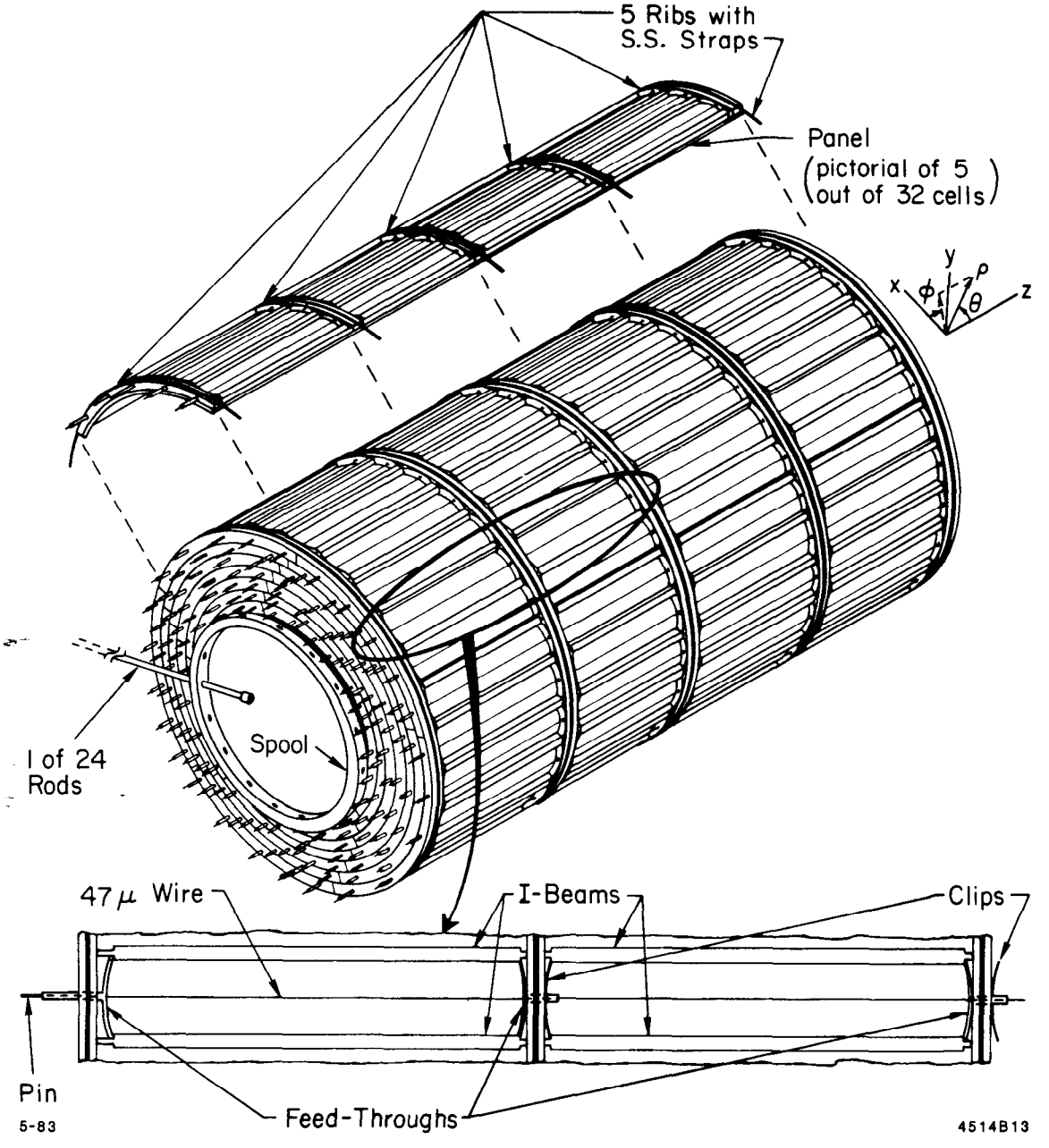
5 Ribs with
S.S. Straps
Panel
(pictorial of 5
out of 32 cells)
y
x
φ
ρ
θ
z
1 of 24
Rods
Spool
47 μ Wire
I-Beams
Clips
Pin
Feed-Throughs
5-83
4514B13

Fig. 19

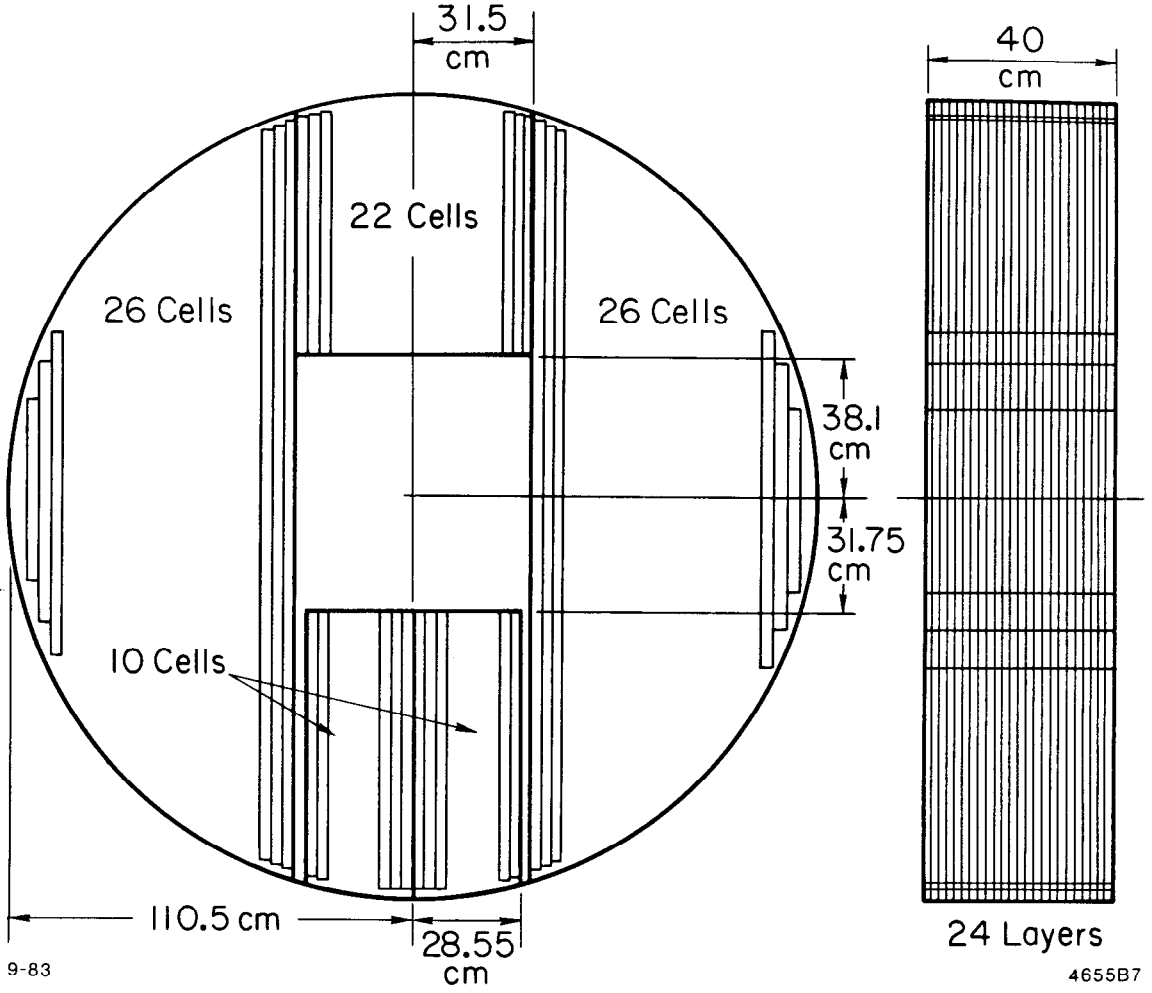
31.5
cm
40
cm
22 Cells
26 Cells
26 Cells
38.1
cm
31.75
cm
10 Cells
110.5 cm
28.55
cm
24 Layers
9-83
4655B7

Fig. 20

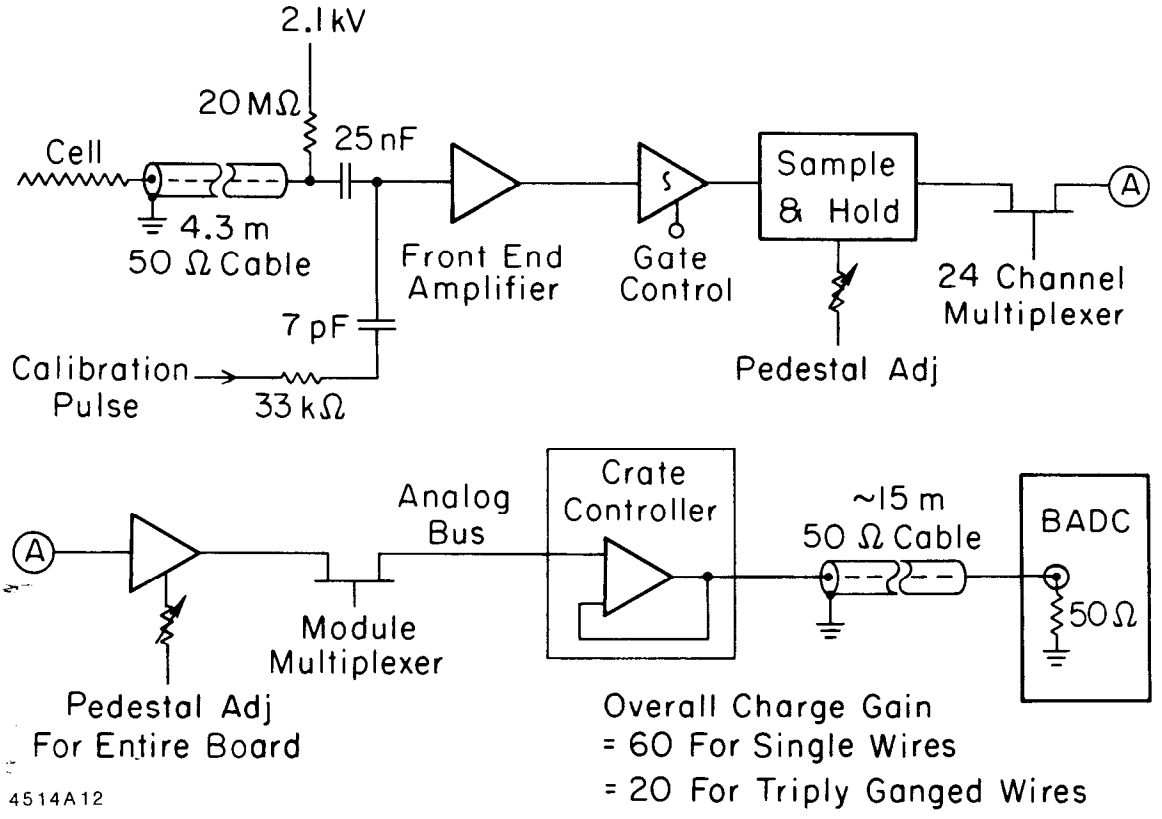
2.1 kV
20 MΩ
25 nF
Cell
4.3 m
50 Ω Cable
Front End
Amplifier
Gate
Control
Sample
& Hold
A
24 Channel
Multiplexer
7 pF
Calibration
Pulse
33 kΩ
Pedestal Adj
A
Analog
Bus
Crate
Controller
~15 m
50 Ω Cable
BADC
50 Ω
Module
Multiplexer
Pedestal Adj
For Entire Board
Overall Charge Gain
= 60 For Single Wires
= 20 For Triply Ganged Wires
4514A12

Fig. 21

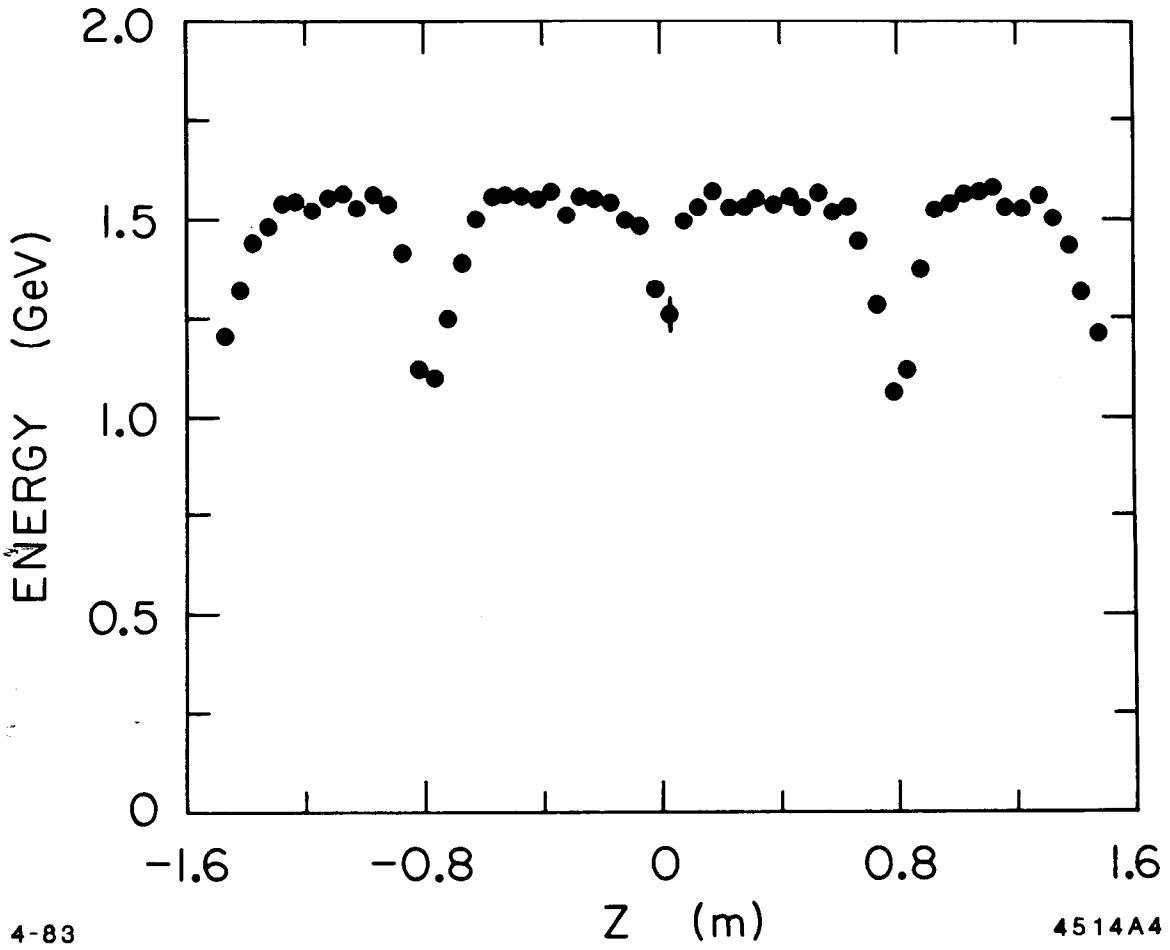

Fig. 22

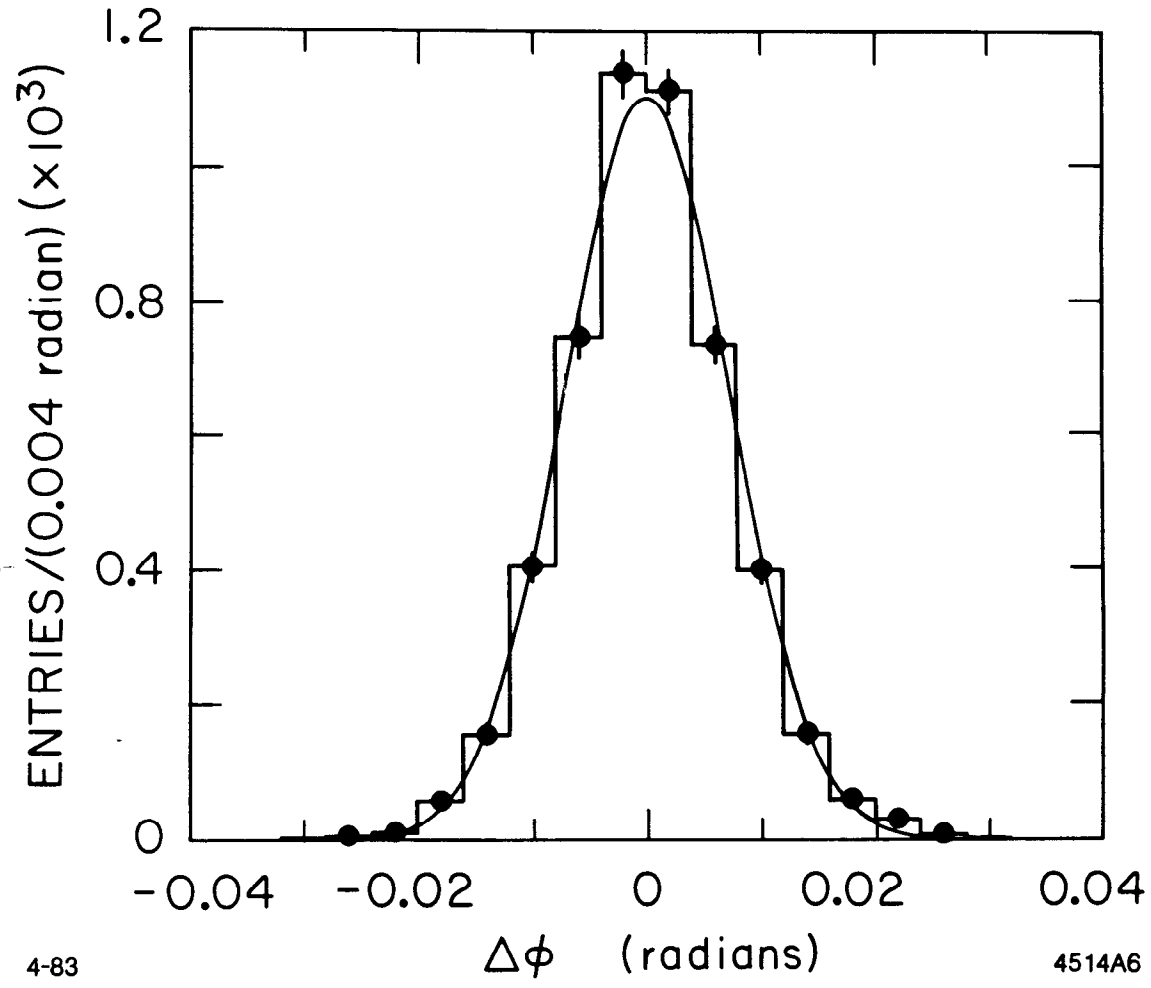
1.2
0.8
0.4
0
ENTRIES/(0.004 radian) (x10³)
-0.04
-0.02
0
0.02
0.04
Δφ (radians)
4-83
4514A6

Fig. 23

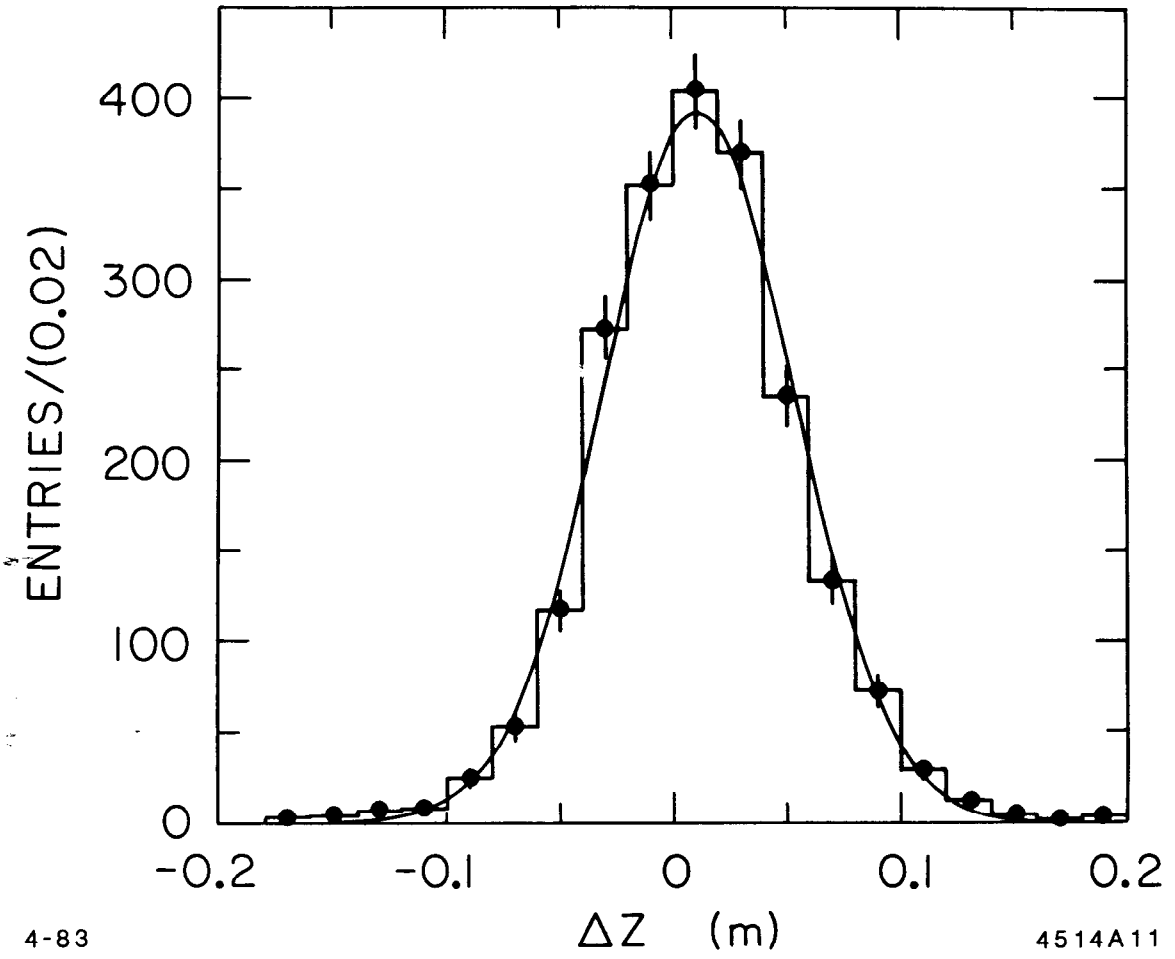

Fig. 24

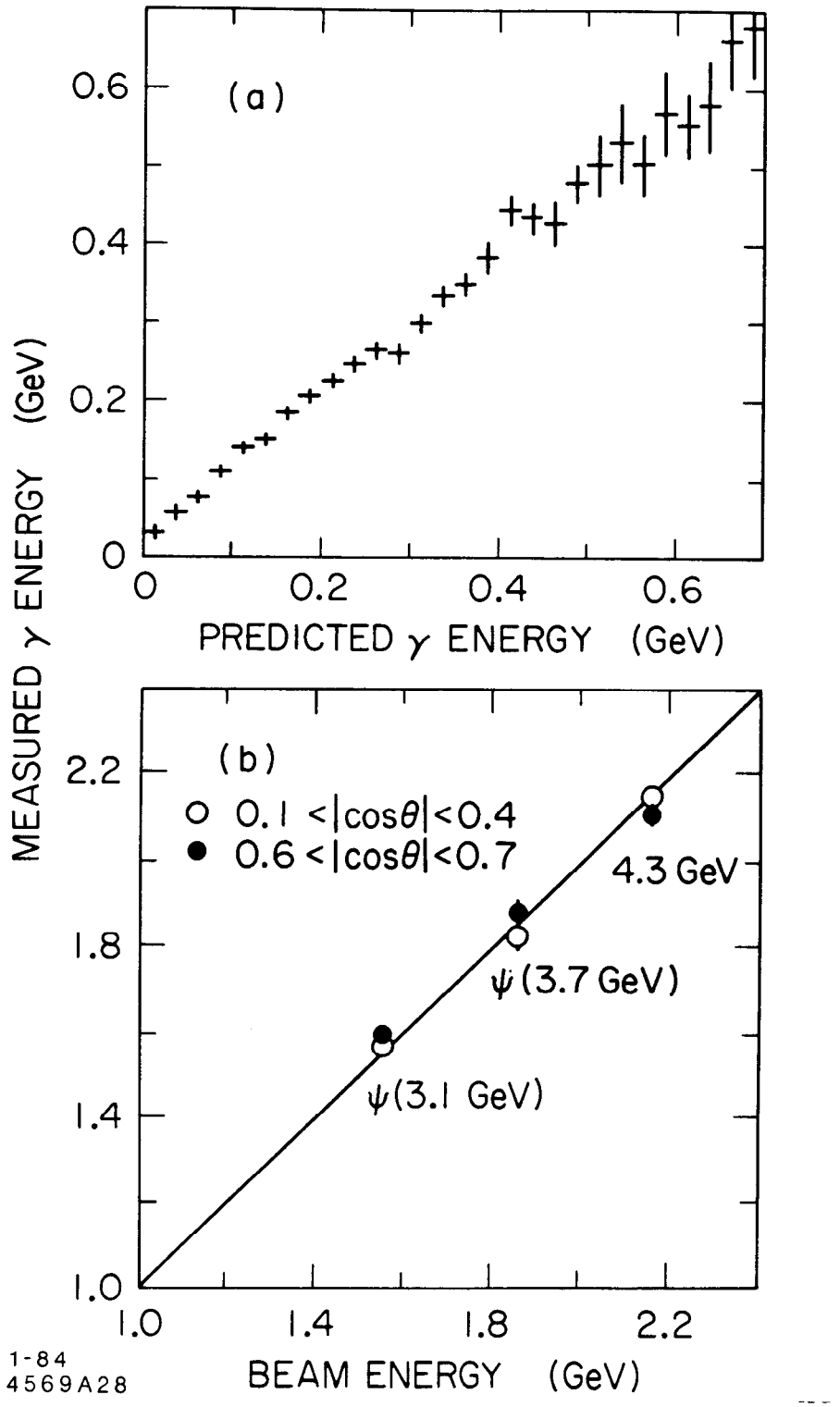
(a)
0.6
0.4
0.2
0
0
0.2
0.4
0.6
MEASURED γ ENERGY (GeV)
PREDICTED γ ENERGY (GeV)
(b)
○ 0.1 <|cosθ|<0.4
● 0.6 <|cosθ|<0.7
4.3 GeV
ψ(3.7 GeV)
ψ(3.1 GeV)
2.2
1.8
1.4
1.0
1.0
1.4
1.8
2.2
BEAM ENERGY (GeV)
1-84
4569A28

Fig. 25

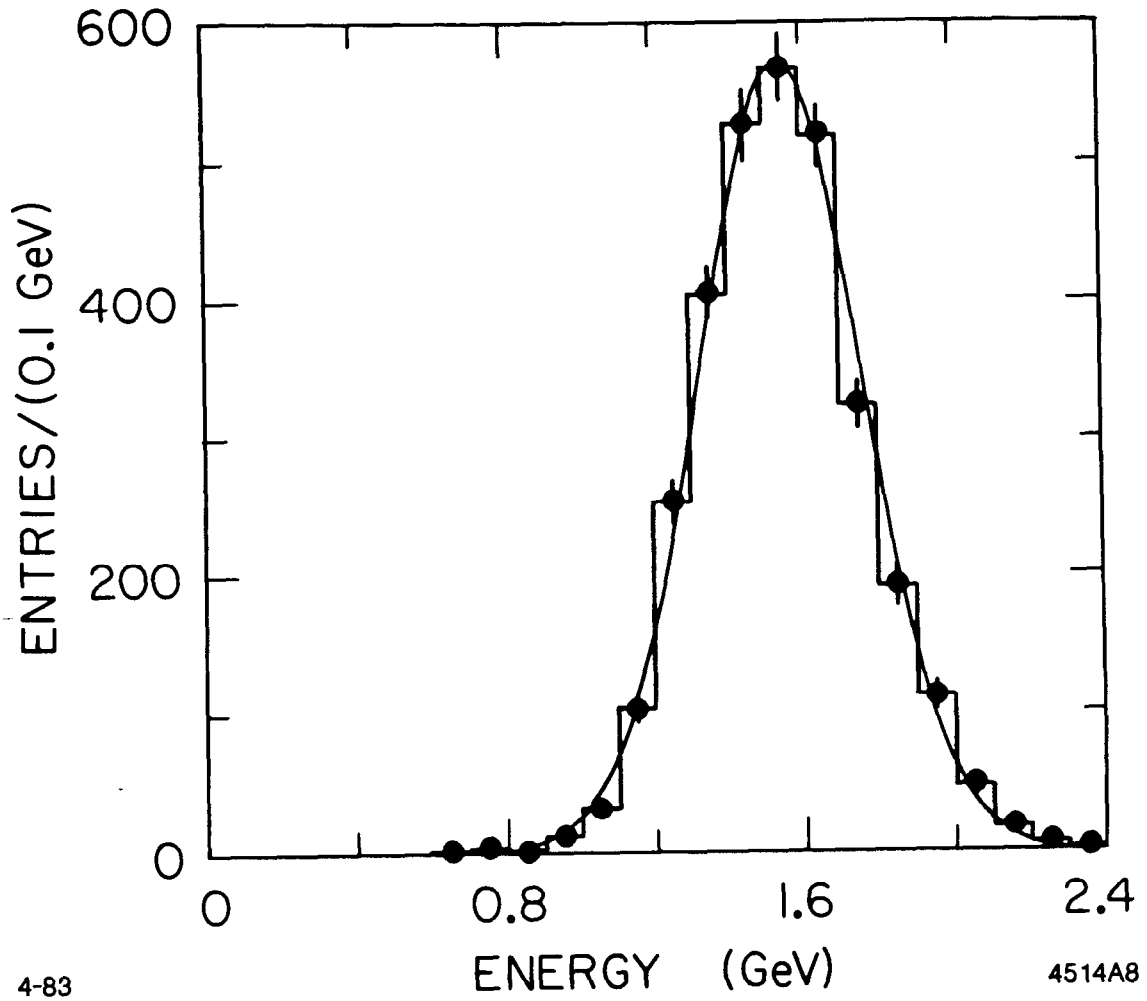

Fig. 26

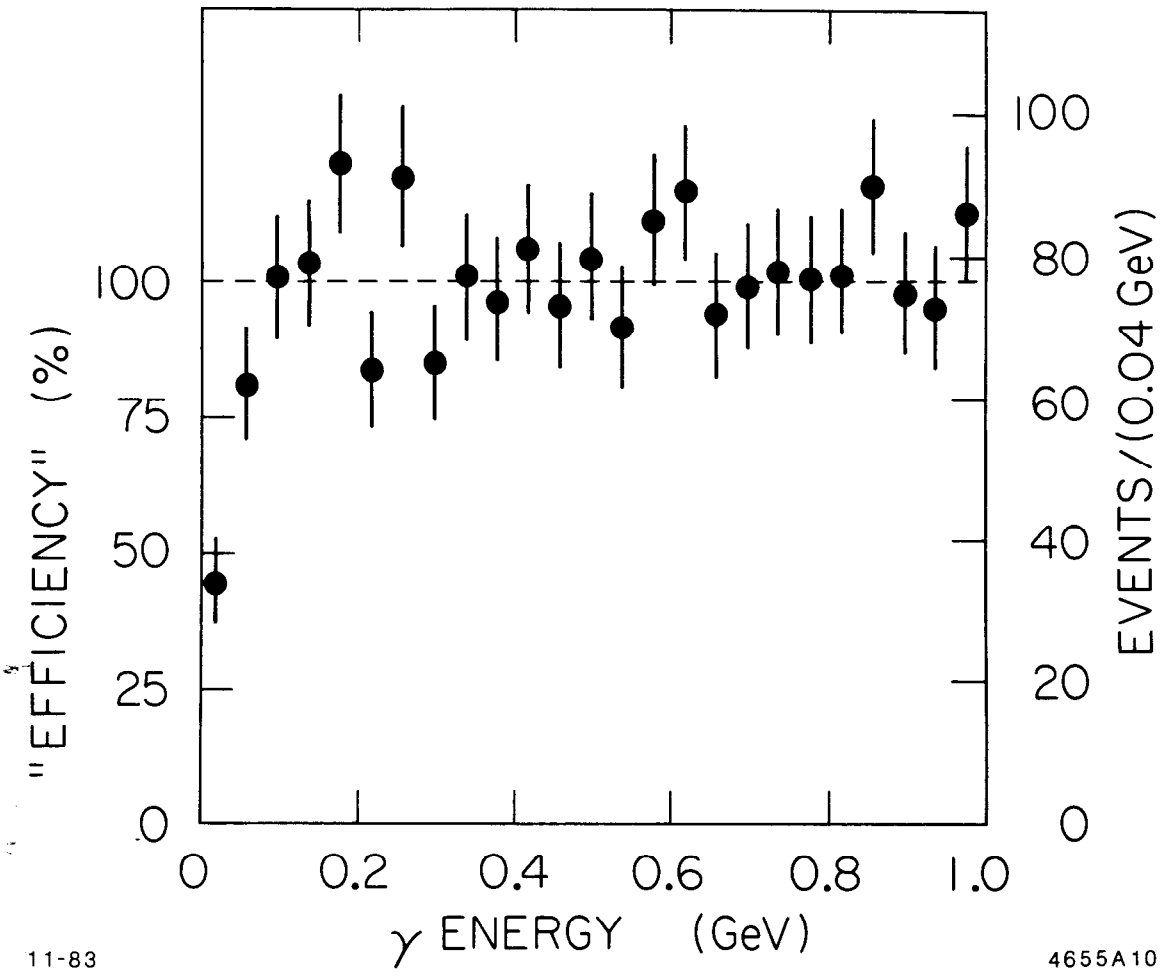
"EFFICIENCY" (%)
100
75
50
25
0
0
0.2
0.4
0.6
0.8
1.0
γ ENERGY (GeV)
EVENTS/(0.04 GeV)
100
80
60
40
20
0
11-83
4655A10

Fig. 27

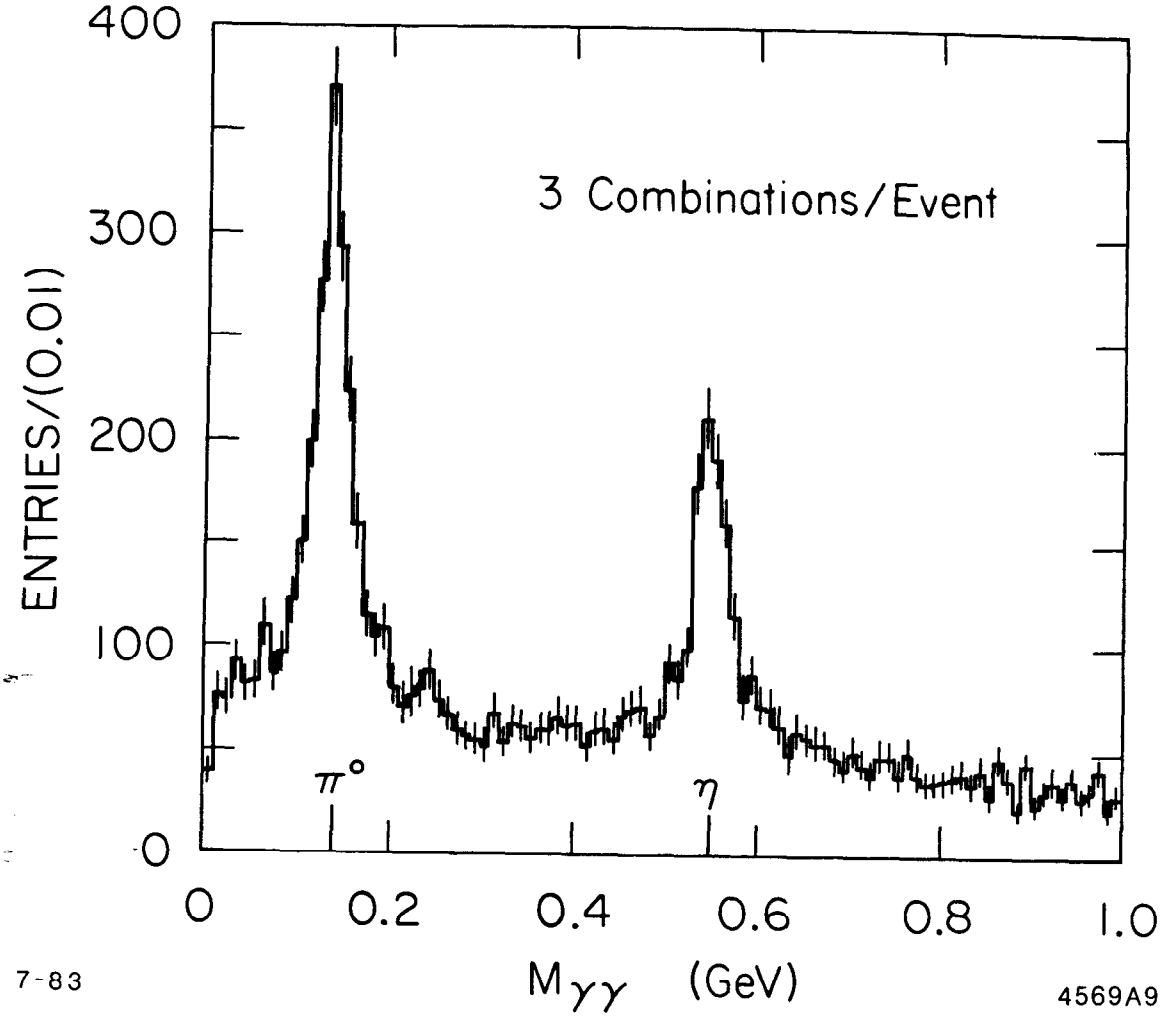
400
300
200
100
0
ENTRIES/(0.01)
3 Combinations/Event
π°
η
0
0.2
0.4
0.6
0.8
1.0
Mγγ (GeV)
7-83
4569A9

Fig. 28

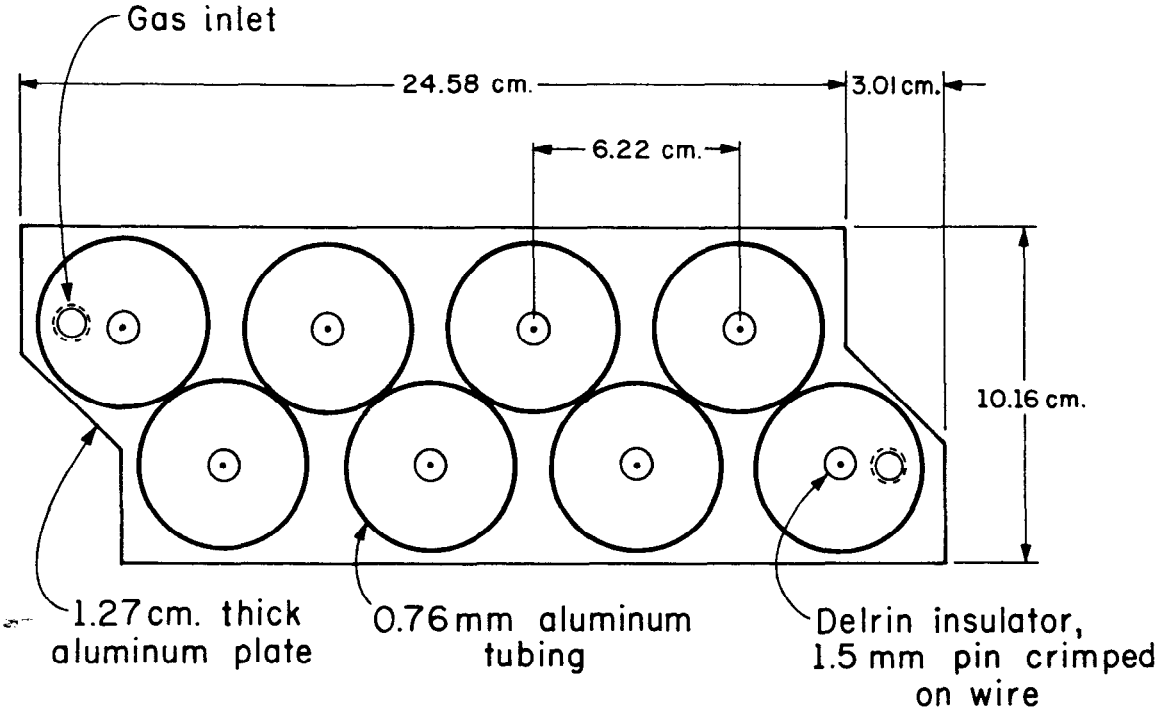

12-83 MUON TUBE ASSEMBLY 4569A27

Fig. 29

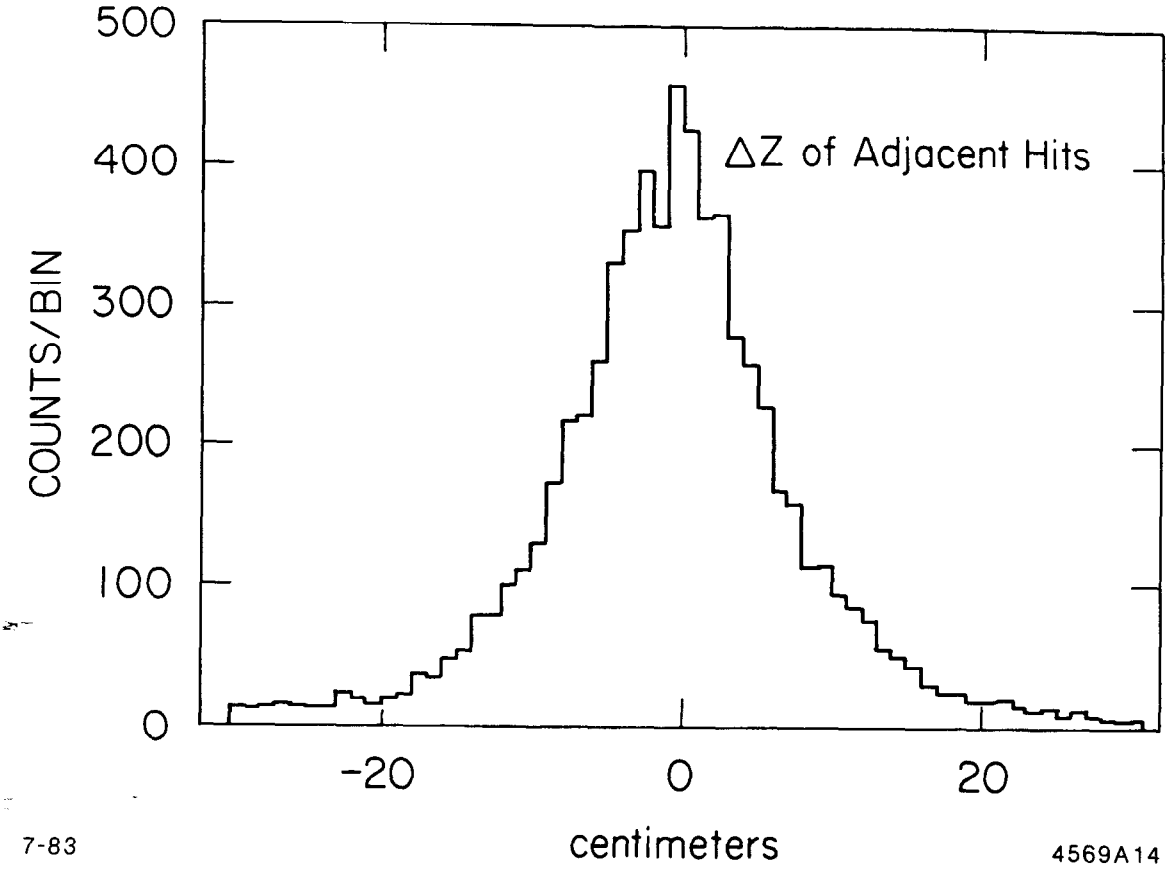
500
400
300
200
100
0
COUNTS/BIN
ΔZ of Adjacent Hits
-20
0
20
centimeters
7-83
4569A14

Fig. 30

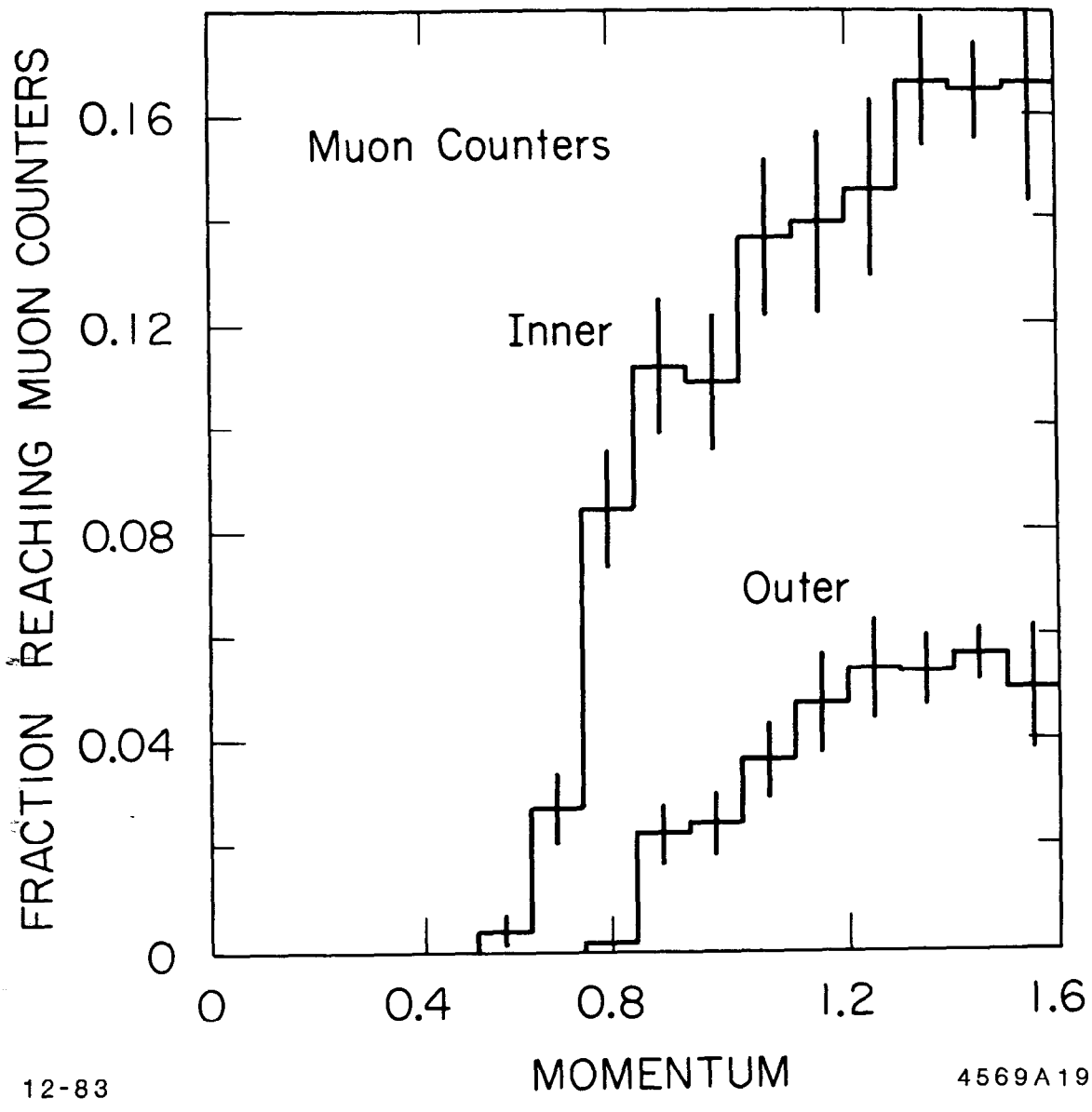
FRACTION REACHING MUON COUNTERS
0.16
0.12
0.08
0.04
0
Muon Counters
Inner
Outer
0
0.4
0.8
1.2
1.6
MOMENTUM
12-83
4569A19

Fig. 31

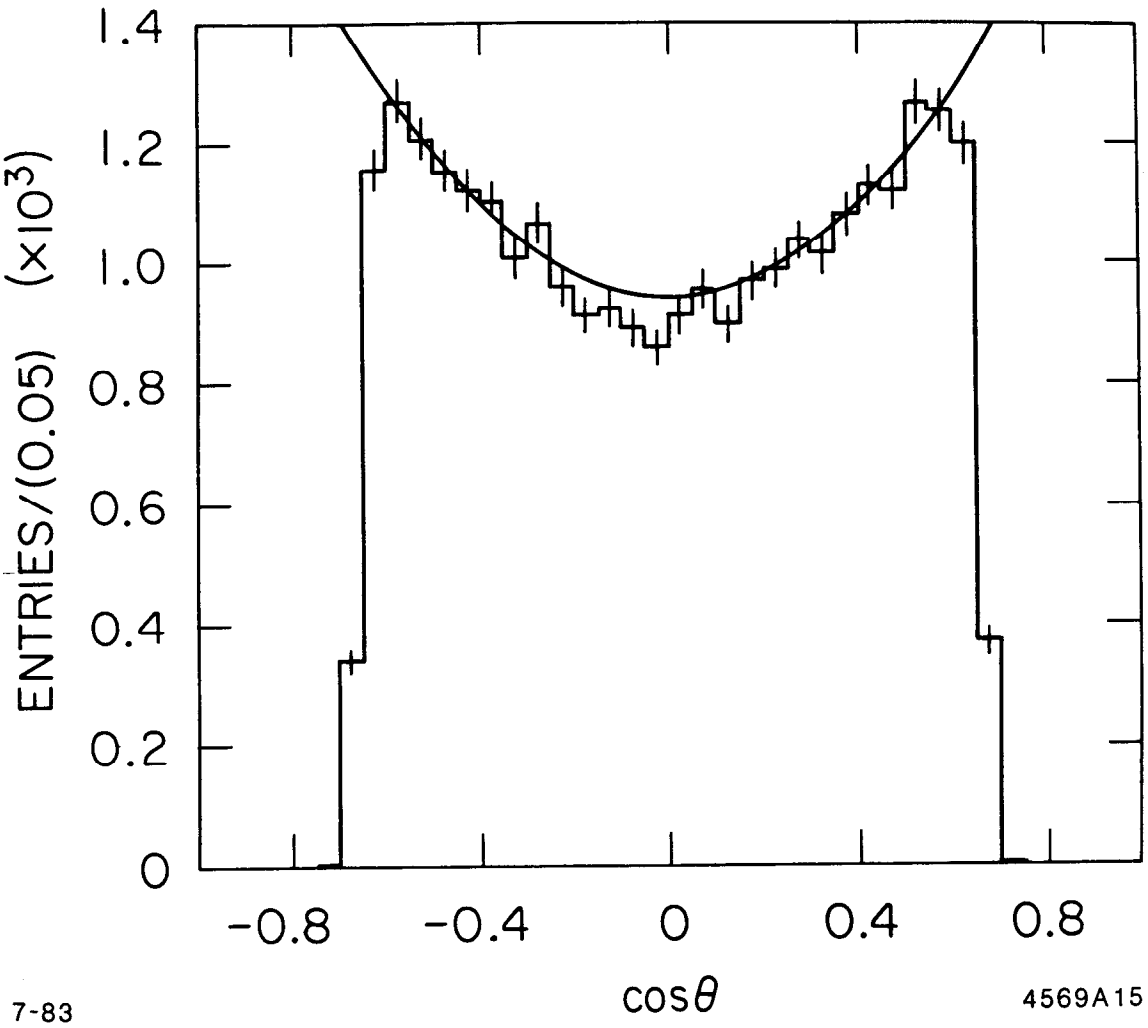
1.4
1.2
1.0
0.8
0.6
0.4
0.2
0
ENTRIES/(0.05) (×10³)
-0.8
-0.4
0
0.4
0.8
cosθ
7-83
4569A15

Fig. 32

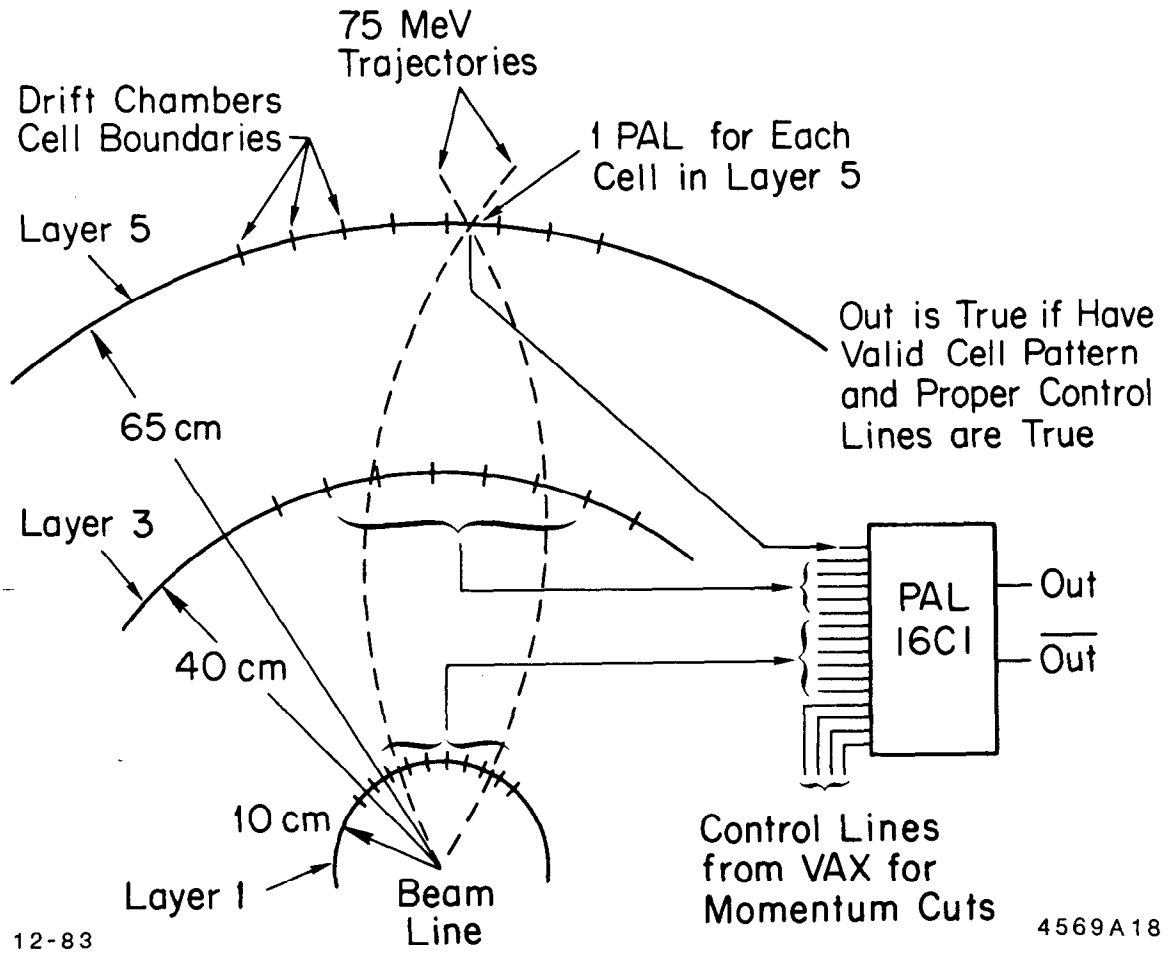
75 MeV
Trajectories
Drift Chambers
Cell Boundaries
1 PAL for Each
Cell in Layer 5
Layer 5
Out is True if Have
Valid Cell Pattern
and Proper Control
Lines are True
65 cm
Layer 3
PAL
16C1
Out
Out
40 cm
10 cm
Layer 1
Beam
Line
Control Lines
from VAX for
Momentum Cuts
12-83
4569A18

Fig. 33

LUMINOSITY MONITOR

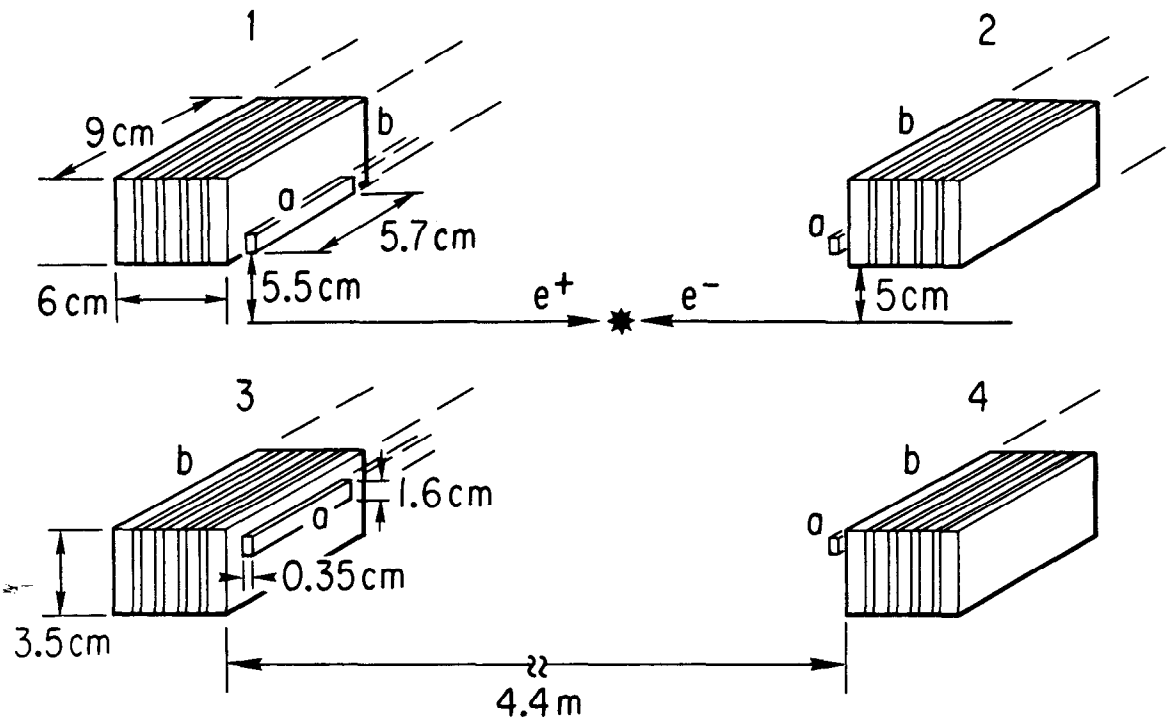

Signal used

1a·1b·4b or 3a·3b·2b

plus

2a·2b·3b or 4a·4b·1b

7 – 83

4569A2

Fig. 34

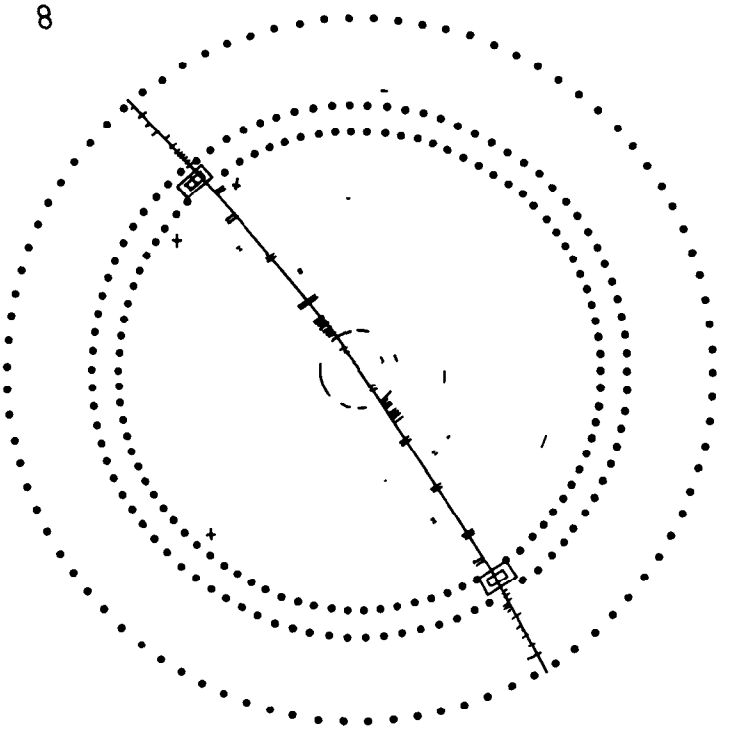

12-83
4569A22

Fig. 35

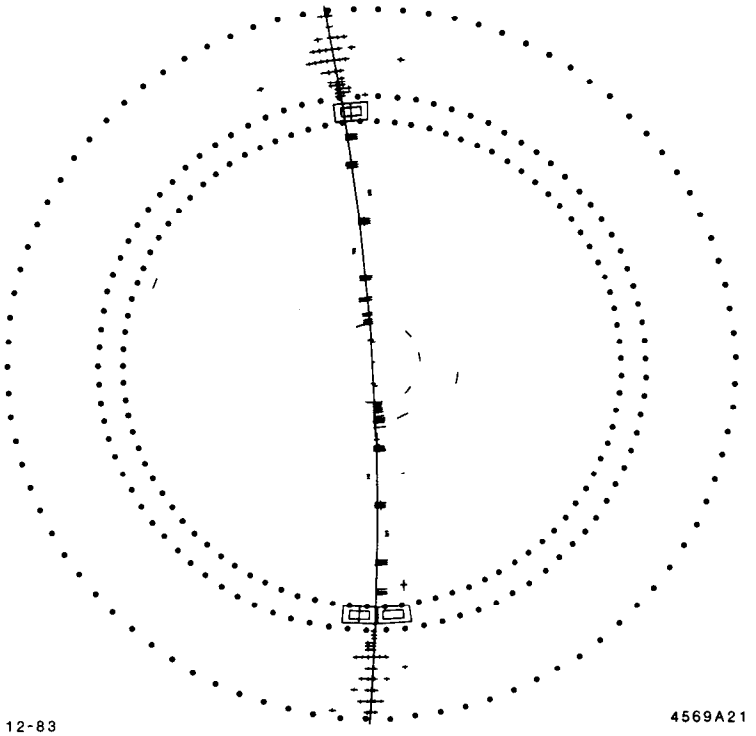

Fig. 36

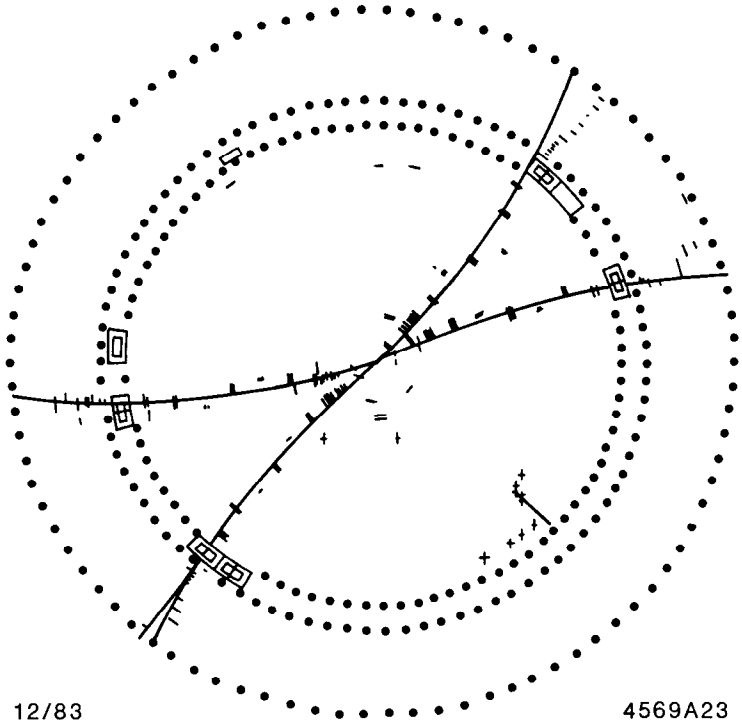

Fig. 37

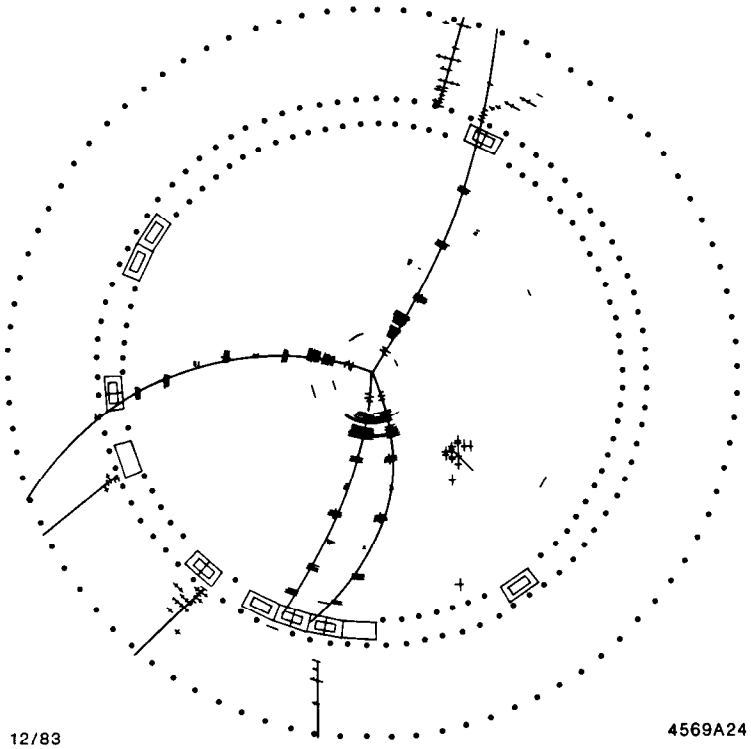

Fig. 38

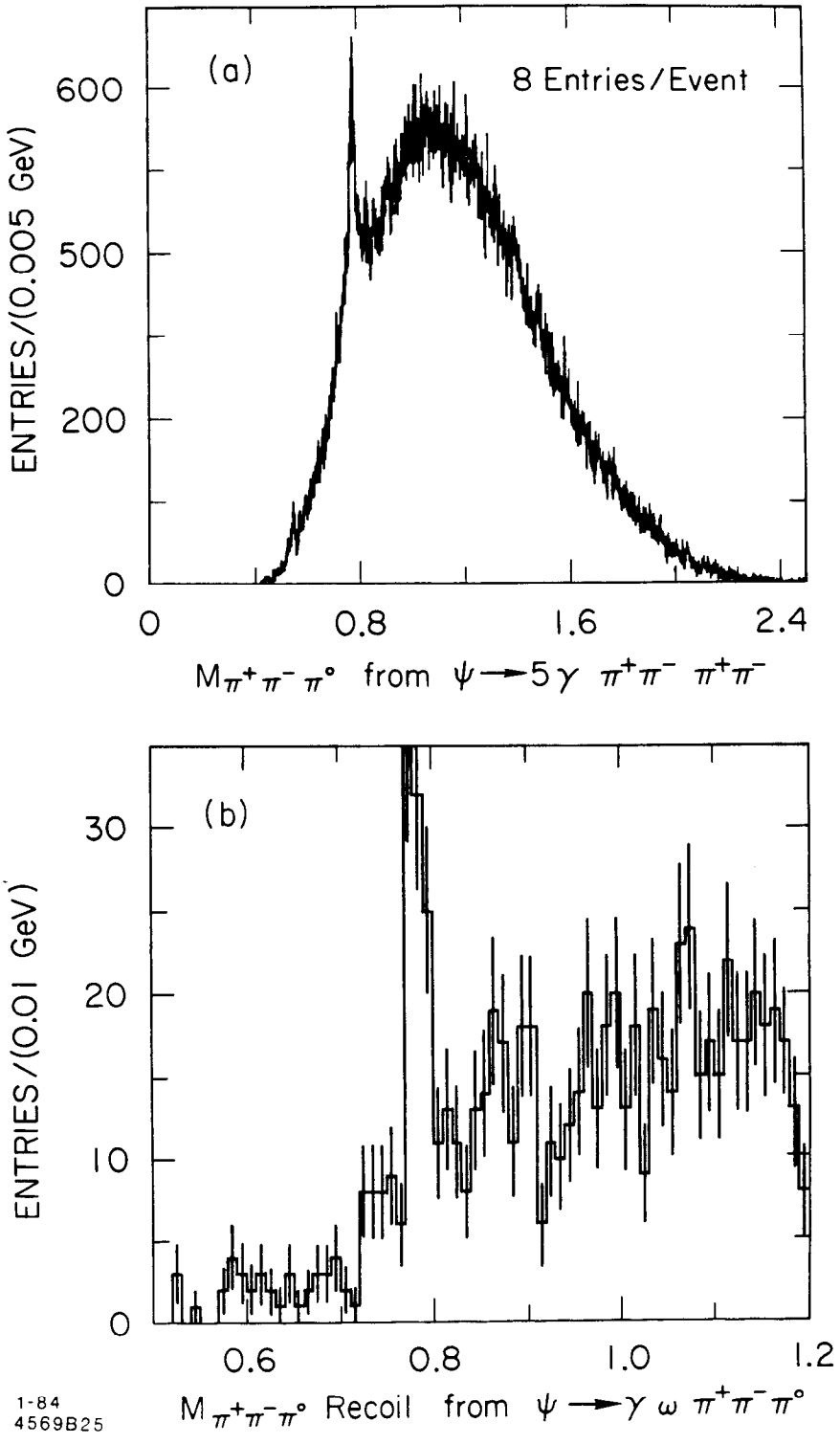
(a)
8 Entries/Event
ENTRIES/(0.005 GeV)
600
500
200
0
0
0.8
1.6
2.4
$M_{\pi^+\pi^-\pi^\circ}$ from $\psi \rightarrow 5\gamma\ \pi^+\pi^-\ \pi^+\pi^-$
(b)
ENTRIES/(0.01 GeV)
30
20
10
0
0.6
0.8
1.0
1.2
$M_{\pi^+\pi^-\pi^\circ}$ Recoil from $\psi \rightarrow \gamma\ \omega\ \pi^+\pi^-\pi^\circ$
1-84
4569B25

Fig. 39

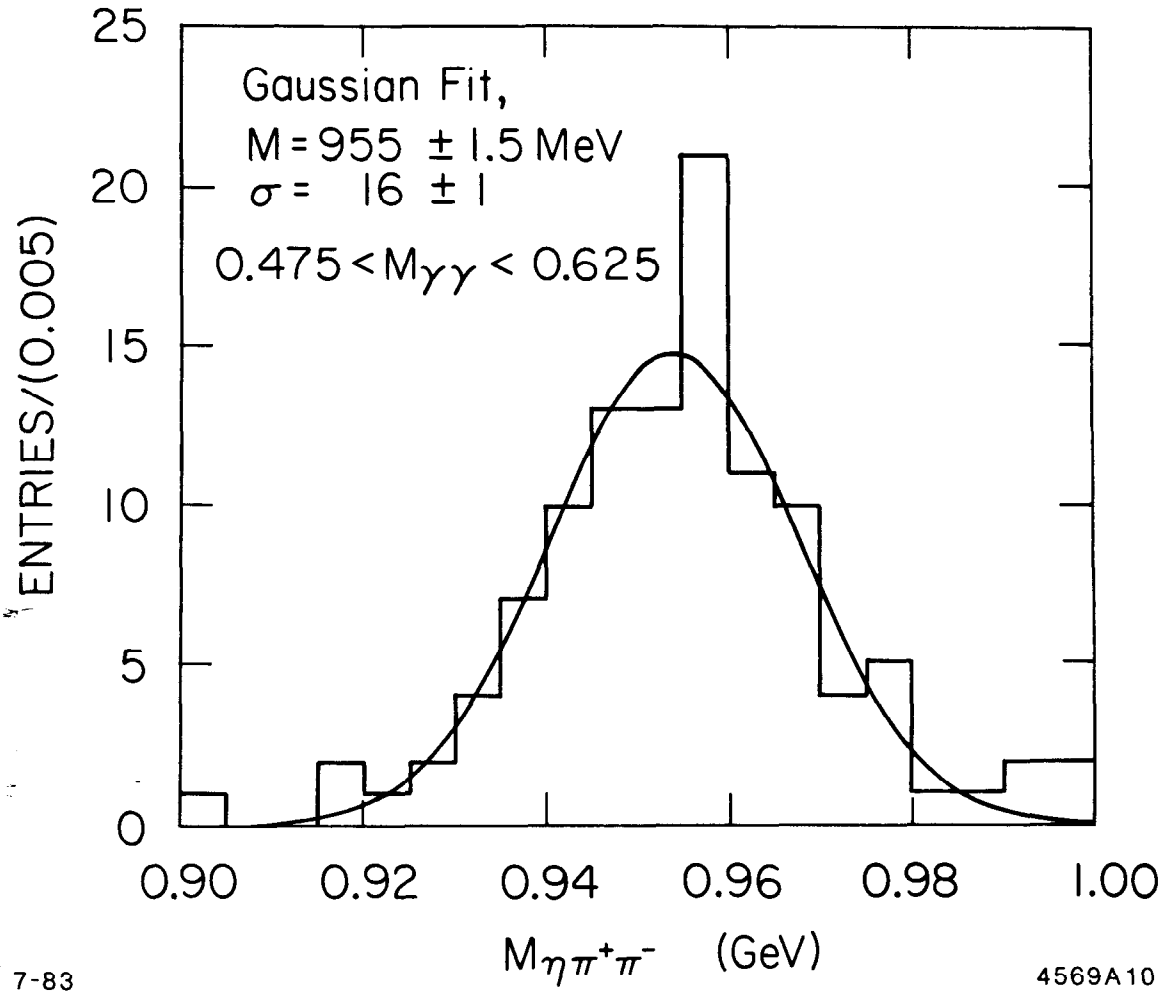
Gaussian Fit,
M = 955 ± 1.5 MeV
σ = 16 ± 1
0.475 < Mγγ < 0.625
ENTRIES/(0.005)
25
20
15
10
5
0
0.90
0.92
0.94
0.96
0.98
1.00
Mηπ+π- (GeV)
7-83
4569A10

Fig. 40

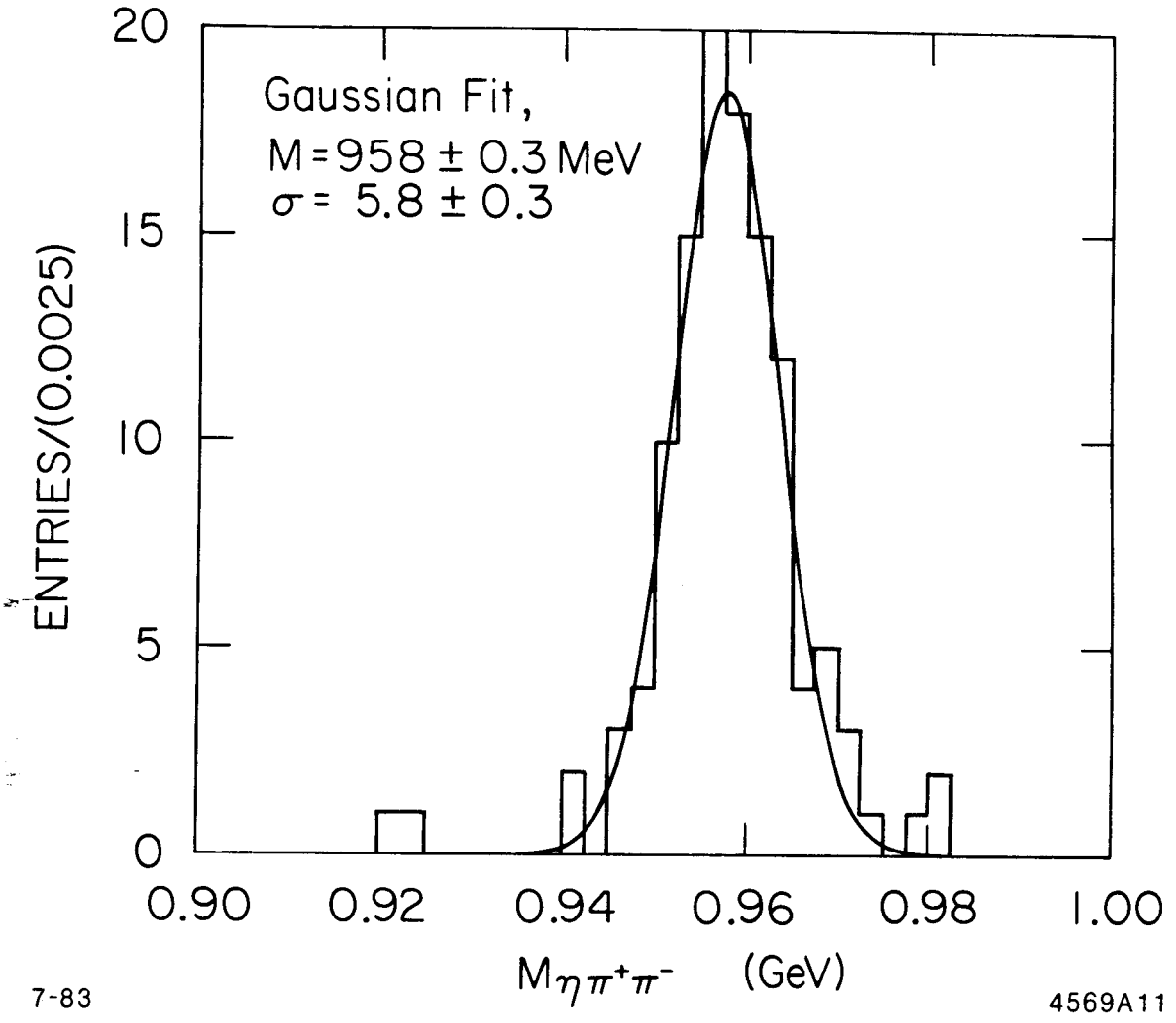
Gaussian Fit,
M = 958 ± 0.3 MeV
σ = 5.8 ± 0.3
ENTRIES/(0.0025)
20
15
10
5
0
0.90
0.92
0.94
0.96
0.98
1.00
$M_{\eta\pi^+\pi^-}$ (GeV)
7-83
4569A11

Fig. 41

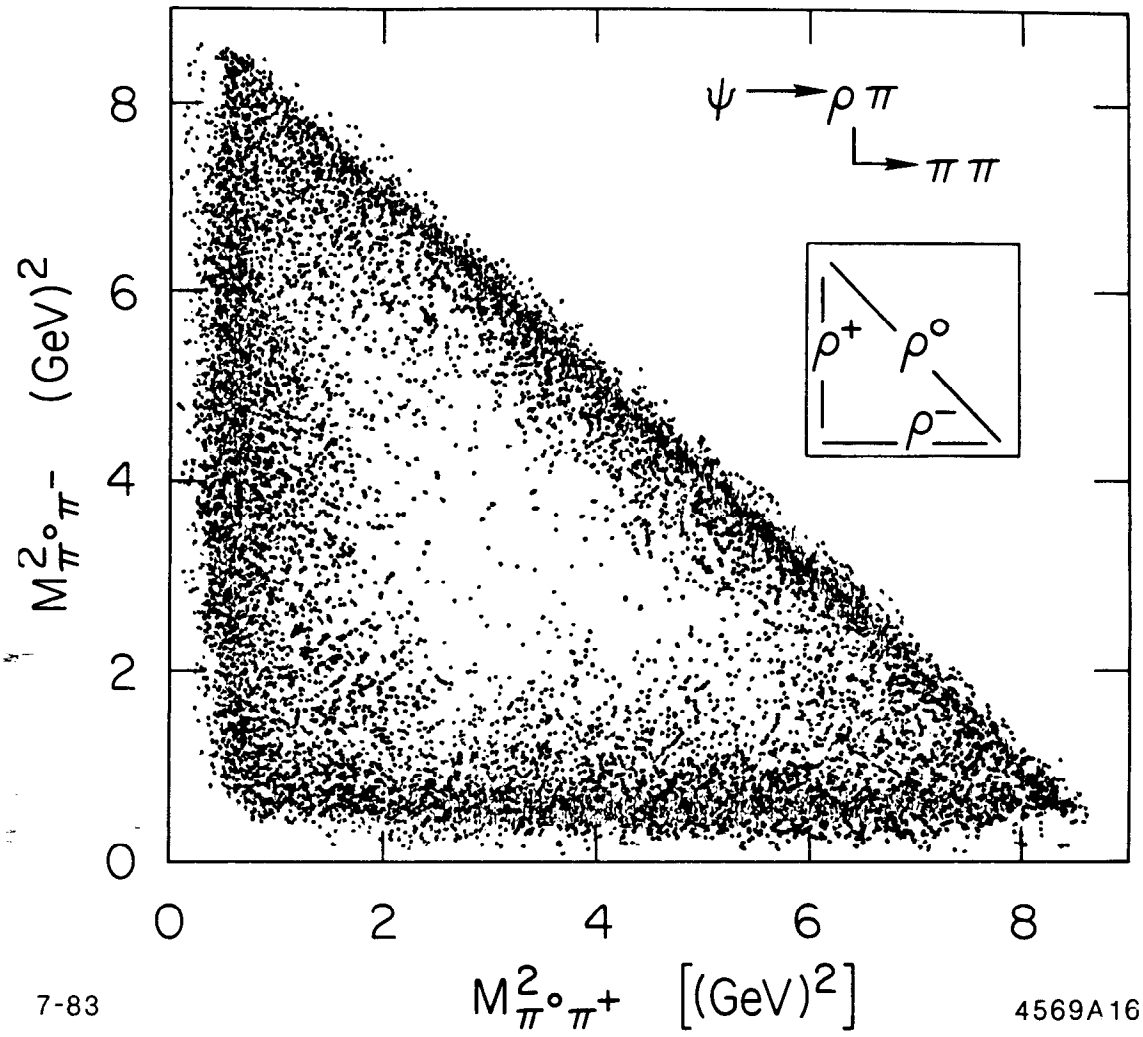
ψ → ρ π
→ π π
ρ+
ρ°
ρ−
$M^2_{\pi^\circ\pi^-}$ (GeV)^2
$M^2_{\pi^\circ\pi^+}$ [(GeV)^2]
0
2
4
6
8
7-83
4569A16

Fig. 42